HHS Public Access

Author manuscript

Cell Rep. Author manuscript; available in PMC 2026 March 11.

Published in final edited form as:

Cell Rep. 2026 January 27; 45(1): 116708. doi:10.1016/j.celrep.2025.116708.

Single-cell resolution of an open chromatin signature in persister tumor cells

Mihai Gabriel Dumbrava[1,2,9], **Wazim Mohammed Ismail**[1,9], **Leticia Sandoval**[1,3], **Amelia Mazzone**[1], **Syed Mohammed Musheer Aalam**[1], **Megan L. Ritting**[1,4], **Xiaonan Hou**[5], **Yiwen Xie**[1,4], **Sierra Hamernick**[1,4], **Chunling Hu**[1], **Fergus J. Couch**[1], **Shariska P. Harrington**[6], **Scott H. Kaufmann**[5,7,8], **Nagarajan Kannan**[1], **S. John Weroha**[5], **Alexandre Gaspar-Maia**[1,10,*]

[1]Division of Experimental Pathology, Department of Lab Medicine and Pathology, Mayo Clinic, Rochester, MN, USA

[2]Mayo Medical Scientist Training Program, Mayo Clinic, Rochester, MN, USA

[3]Department of Internal Medicine, Mayo Clinic School of Graduate Medical Education, Scottsdale, AZ, USA

[4]Mayo Clinic Graduate School of Biomedical Sciences, Mayo Clinic, Rochester, MN, USA

[5]Division of Oncology Research, Department of Oncology, Mayo Clinic, Rochester, MN, USA

[6]Department of Obstetrics and Gynecology, Mayo Clinic, Rochester, MN, USA

[7]Department of Molecular Pharmacology and Experimental Therapeutics, Mayo Clinic, Rochester, MN, USA

[8]Division of Hematology, Department of Medicine, Mayo Clinic, Rochester, MN, USA

[9]These authors contributed equally

[10]Lead contact

SUMMARY

Cancer can recur when a subset of tumor cells, termed persister cells, survive therapy and re-enter the cell cycle. Through single-nucleus multi-omic profiling (single-nucleus RNA sequencing [snRNA-seq] and single-nucleus assay for transposase-accessible chromatin by sequencing [snATAC-seq]) of (1) non-malignant fallopian tubes and (2) treatment-naive and (3) neoadjuvant-chemotherapy-treated samples from patients with high-grade serous ovarian carcinoma (HGSOC), we identify a persister cell signature defining the chemotherapy-tolerant state. The chromatin

*Correspondence: maia.alexandre@mayo.edu.

AUTHOR CONTRIBUTIONS

A.G.-M., W.M.I., M.G.D., and L.S. conceived and designed the study. L.S., M.G.D., A.M., and S.H. performed the experiments and tumor sample collection. X.H. and S.J.W. performed the mouse work. M.L.R., S.M.M.A., and N.K. provided the FT tissue. M.G.D., S.P.H., and S.H.K. curated the patient tumor cohort and clinical data. C.H. and F.J.C. performed the targeted DNA sequencing. W.M.I. and M.G.D. performed the data analysis with the help of Y.X. and A.G.-M. M.G.D. wrote the manuscript with the help of W.M.I. and A.G.-M. All authors critically revised and approved the final version of the manuscript.

DECLARATION OF INTERESTS

The authors declare no competing interests.

features of the signature are detectable in residual tumors after treatment and in treatment-naive tumors from patients who later develop resistance. Further, the signature independently predicts chemotherapy response in metastatic HGSOC and patient-derived xenograft models. Cells enriched in the persister state display a subset of genes primed for expression before treatment, an altered cell cycle, and stress-response programs associated with poor clinical outcomes. These findings suggest that an intrinsic regulatory program primes tumor cells toward chemotherapy tolerance and reveal new vulnerabilities that can be targeted with chromatin-modifying agents to prevent cancer recurrence.

Graphical abstract

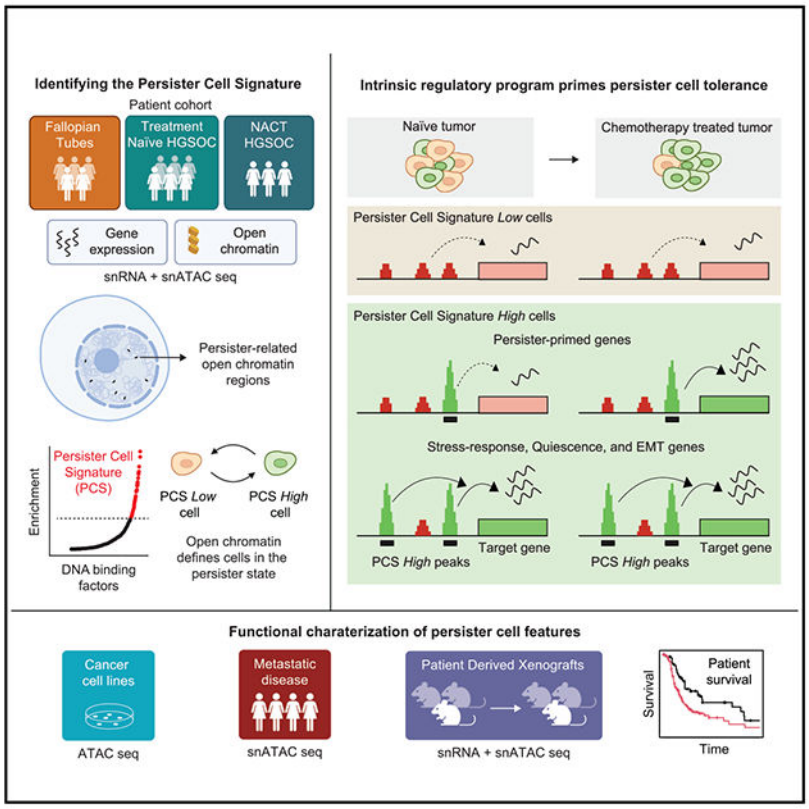

In brief

Dumbrava et al. identify a signature of drug-tolerant persister cells in high-grade serous ovarian carcinoma using chromatin accessibility and transcriptome single-nucleus profiling. Patient tumors with features of the persister cell signature are predisposed to drug tolerance and poor responses to chemotherapy treatment.

INTRODUCTION

High-grade serous ovarian carcinoma (HGSOC) is the most common and lethal subtype of ovarian cancer. At the time of detection, most patients with HGSOC present with advanced-stage disease (III/IV) that has already metastasized to the pelvis and abdomen, resulting in

a 5-year survival rate below 30%.[1] The treatment strategy for HGSOC typically consists of radical debulking surgery combined with an adjuvant or neoadjuvant platinum and taxane chemotherapy regimen.[2] However, despite advances in surgical debulking and targeted therapy, patient outcomes remain poor due to the development of recurrent, chemoresistant disease.[3] Since the standard of care is generally the same for most patients, HGSOC becomes a valuable model to study the chemotherapy response. Emerging evidence has highlighted the critical role of non-genetic mechanisms as drivers of cancer progression and therapeutic resistance, including the ability of a subset of cancer cells to adopt a drug-tolerant persister state.[4–6] These epigenetic features modulate transcriptional programs and cellular functions without modifying the underlying DNA sequence. Although persisters are believed to arise from multiple cellular lineages, the precise mechanisms that confer this state and enable these cells to tolerate standard therapies remain poorly understood in HGSOC.

Persister states in cancer may be mediated by the rewiring of transcriptional programs rather than stable genetic changes. The interplay between lineage-specific master transcription factors (TFs) and chromatin remodelers has been implicated in maintaining these states across various malignancies. Recently, the TFs MECOM, PAX8, SOX17, and WT1 were identified to have cooperative DNA-binding patterns that are rewired to promote pro-oncogenic signaling in HGSOC.[7] Tumor-specific modifications to the chromatin landscape have also been established across female malignancies with implications for cellular reprogramming and activation of oncogenic programs.[8]

Non-coding regions are an integral part of the regulatory information and contribute profoundly to tumor biology.[9,10] It has become increasingly evident that regulatory elements (i.e., *cis*-acting enhancers) are rewired in cancer cells to promote growth, survival, and other aggressive phenotypes associated with poor clinical outcomes.[11–13] Previous studies have used transcriptomic and epigenomic approaches to characterize the molecular heterogeneity of HGSOC, revealing extensive variation in regulatory mechanisms.[7,11,14] However, most have relied on bulk genomic sequencing of material collected from heterogeneous mixtures of different cell types and from cell lines, obscuring cancer cell-specific activity of oncogenic enhancers. Single-cell genomics has revolutionized our ability to explore cellular heterogeneity of ovarian tumors, yet the characterizations have been predominantly based on transcriptomes via single-nucleus RNA sequencing (snRNA-seq).[15–19] The single-nucleus assay for transposase-accessible chromatin by sequencing (snATAC-seq)[20,21] performs high-throughput profiling of chromatin accessibility, revealing complex facets of gene regulation. Recently, scATAC-seq has allowed for analysis of the chromatin accessibility of ovarian cancer omental metastases, identifying profound tumor heterogeneity post-chemotherapy and an association between stress responses and chemoresistance.[22] Together, gene expression (GEX) and ATAC enable the linking of regulatory elements to putative target genes at single-cell resolution, offering key mechanistic insights into the molecular basis of the drug response and potentially predicting persister states. Here, we present a cohort of patients with ovarian cancer profiled by simultaneous transcriptomic and chromatin accessibility sequencing from the same nuclei, revealing novel insights into the regulation of key oncogenic pathways.

In this study, we sought to characterize the chromatin landscape and transcriptional features of persister cells in HGSOC. We performed single-nucleus multi-omic profiling (snRNA+ snATAC seq) of isolated nuclei from (1) non-malignant fallopian tubes (FTs) as well as (2) treatment-naive and (3) neoadjuvant-chemotherapy (NACT)-treated tissues from patients with HGSOC and (4) patient-derived xenograft (PDX) models from patients with HGSOC. This approach enabled us to identify a distinct epigenetic signature of persister cells that distinguished the chemotherapy response in treatment-naive tumors, indicating that the persister potential is encoded in a chromatin landscape. Importantly, this persister cell signature (PCS) also successfully predicted the chemotherapy response in an experimental PDX model and metastatic ovarian cancer. Together, these findings reveal an intrinsic epigenetic program underlying chemotherapy tolerance and identify new vulnerabilities that could be exploited to delay or even prevent ovarian cancer recurrence.

RESULTS

Transcriptomic and epigenomic landscape of FTs and HGSOC

To characterize the transcriptomic and epigenomic landscape of HGSOC, we performed single-nucleus multi-omic profiling of GEX and open chromatin from ATAC-seq using the 10× Genomics platform. Our cohort consisted of tumor samples collected after debulking surgery from 9 patients with HGSOC (6 at the time of primary debulking surgery, who are designated as treatment naive, and 3 at the time of interval debulking after NACT, who are designated as “NACT patients”) (Figure 1A). All tumors were histologically classified as high grade, and the patients who received NACT prior to acquisition of the debulking surgery specimen were classified as minimally or partially responsive to therapy based on their chemotherapy response scores (CRSs; range: 1–2) (Figures 1B and S1A). Of the 6 treatment-naive patients, 3 patients were found to be sensitive to adjuvant chemotherapy, and the other 3 patients were resistant based on recurrence within 6 months of the last cycle of chemotherapy. Since debulking status could be a confounding factor for recurrence, we selected only naive tumors with optimal debulking. Furthermore, we sequenced histologically normal FT tissues with ostensibly normal cells from a cohort of 5 patients who underwent salpingectomy as a control group (hereafter referred to as non-malignant FTs).[7,23] The oncoprint shows the mutational status of each patient for a panel of selected genes associated with homologous recombination (HR) repair machinery and the clinical characteristics of the cohort (Figure 1B; Table S1).

After rigorous quality control (Figures S1B and S1C), we obtained high-quality multi-omic data for 52,864 cells (Figure 1C). Mitochondrial DNA variant analysis[24] confirmed the single clonal origin of these tumors in each patient (Figure S2A). Cell types were identified using an unsupervised clustering and reference-mapping approach, followed by marker validation from GEX, chromatin accessibility, and integration of GEX and ATAC data (Figures 1C, 1D, and S2B). As expected, the immune cells, stromal cells, and non-malignant epithelial cells from the FT samples clustered together by cell type, while the malignant cells (epithelial cells from the tumor samples) clustered by individual patient, as these cells are likely to be genetically more similar to each other than any other cell type. Tumor samples primarily comprised malignant epithelial cells and had decreased infiltration of immune and

stromal cells compared to FTs (Figure 1E). Global changes in open chromatin (cut sites) could be characterized by two main observations: (1) a decreasing trend in the chromatin accessibility of immune cells from FT to naive tumors and then to NACT tumors and (2) a general increasing trend in open chromatin sites in endothelial cells, fibroblasts, and epithelial cells from naive tumors to NACT tumors (Figure S2C).

Sub-classification of epithelial cells from normal and malignant patient samples

To identify epithelial subpopulations that were distinct in their GEX profiles, we subclustered the epithelial cells (Figure S2A) after applying batch-correction methods to remove the influence of patient covariate (Figure 2A). Estimation of copy-number variation (Figure 2B)[25] to infer changes in genomic structure confirmed high genetic variation in the malignant epithelial cells from HGSOC tumor samples. By overlapping the list of markers identified in distinct clusters with markers from Ulrich et al.[26] and Vasquez-Garcia et al.,[15] we were able to identify cycling, ciliated, and secretory cell subpopulations (Figures 2C and 2D). Three other clusters (1–3) were mainly tumor specific. The top markers for each epithelial cluster (Figure 2E) and the Human Primary Cell Atlas (HPCA) reference-mapping scores (Figure S3B) suggest the most likely cell types for each cluster. FT samples mostly comprised ciliated and secretory epithelial cells, as expected, while the naive tumors had the most cycling cells (Figure 2F). Comparison with canonical cell cycle markers supported the epithelial subcluster identification, such that cycling cells had the highest G2/mitosis phase (G2M) score (Figure 2G). We observed reduced numbers of cycling cells in NACT tumor samples, reflecting the fact that chemotherapy targets cycling cells. Co-accessibility analysis using snATAC data showed that the markers for ciliated (FOXJ1) and secretory (MSLN)[26] cells demonstrate increased co-accessibility in their respective cell types, corresponding directly to their increased GEX in FTs (Figure 2H), confirming that *cis*-regulatory interactions can be inferred from the snATAC data. Interestingly, most of these interactions are also maintained in tumors, indicating that the regulatory networks for genes involved in cell identity are similar to FTs (Figure S3C).

Characterizing the transcriptomic and epigenomic programs of HGSOC

Most cases of HGSOC are thought to arise from the FTs.[7,23] To identify molecular changes driving malignant transformation, we compared transcriptomic and epigenomic profiles of FT and treatment-naive tumor samples (Figure 3A). Cell-type-specific differential expression analysis comparing HGSOC naive and FT samples (Figure 3B; Table S2) revealed that, globally, there were more genes upregulated in epithelial cells and fibroblasts and fewer genes upregulated in macrophages compared to downregulated genes. Several established ovarian cancer master TFs (MTFs), including MECOM, ESR1, WT1, and PAX8, were upregulated in naive (malignant) epithelial cells, corroborating their role in HGSOC (Figure 3B).[7] We also identified a significant increase in the macrophage-to-monocyte ratio between FTs and naive tumors, suggesting myeloid lineage changes during cancer progression, as previously shown (Figure S4A).[16] Pathway analysis revealed that cancer-related processes were upregulated in naive tumors, including changes in cell cycle genes. In contrast, FTs displayed an enrichment of inflammatory signaling pathways and tumor-suppressor responses (Figure 3C).

We next examined chromatin accessibility changes associated with malignant transformation. Enrichment of binding sites of known DNA-binding factors (DBFs), including TFs and chromatin regulators in each cell, was estimated from the snATAC data.[27] Analyzing the top DBFs enriched in each cell type revealed that there was an altered open chromatin landscape between FTs and naive tumors that was most pronounced in the epithelial cells (Figure S4B). A pairwise correlation analysis between the top epithelial DBFs revealed a cooperative DNA-binding pattern in both FTs and tumors (Figures S4C and S4D), suggesting that these factors may be working together to orchestrate the changes that occur during oncogenesis. The known regulators of ovarian cancer, SOX17, PAX8, WT1, and MECOM, are highly correlated in both FTs and cancer, but SOX17 shifts its cooperativity to oncogenic programs driven by other SOX family members in the malignant state. The AP-1 TF FOSB gains stronger correlations with MECOM, PAX8, and WT1 in tumor cells, suggesting that stress-adaptive mechanisms might reinforce oncogenic transcriptional programs.

To understand the regulatory relationships between TFs and their target genes in malignant and non-malignant states, we used functional inference of gene regulation (FigR)[28] analysis to predict gene regulatory networks (Figure 3D) in FT and naive tumor samples. The KLF family, AP-1 TFs, established drivers of ovarian cancer progression (PAX8, WT1, and FOXM1), and hormonal signaling TFs (ESR1 and PGR) orchestrate many of the changes in GEX between FT and naive tumors. Globally, naive tumors exhibited an increased number of repressive TF-target interactions compared to FTs (Figure 3E). Among the TFs with shared activity in both contexts, we observed that some TFs shift from an activating to a repressive role between FTs and naive tumors, and vice versa (Figure 3F; Tables S3 and S4). These include ATF3, PGR, FOXM1, NR2F1, and ZEB2, which had repressive roles in FT and became activators in tumors. In contrast, BACH2, IRF1, RUNX3, STAT4, WT1, and ESR1 shifted from being activators in FTs to repressors in naive HGSOC. Together, these changes in TF activity and cooperation may orchestrate changes in GEX that are involved in the development of HGSOC.

Comparison of NACT patients and adjuvant-chemotherapy-resistant patients revealed a PCS

To identify transcriptomic and epigenomic markers of chemotherapy resistance, we devised two comparisons: (1) a comparison between treatment-naive patients vs. NACT-treated patients and (2) within the treatment-naive patients, a comparison between patients that developed sensitivity vs. resistance to adjuvant chemotherapy (Figure 4A). We reasoned that a molecular signature leading to chemotherapy resistance could have features similar to residual tumors that survived NACT.

We first analyzed the differentially expressed genes in NACT epithelial cells compared to treatment-naive epithelial cells (Figures 4B and 4C). These were overlapped with known gene signatures established for predicting patient prognosis,[29,30] poor chemoresponses,[19,31] MTFs known to be drivers of ovarian cancer,[4] markers of molecular subtypes of ovarian cancer,[29] and markers of evolutionary states in HGSOC[32] (Table S5). We found that poor chemoresponse and stress-associated gene signatures were significantly enriched in

NACT-upregulated genes, while proliferative signatures were significantly enriched in naive-upregulated genes. Hallmark pathway analysis revealed that pathways related to the cell cycle were downregulated in residual NACT tumors, as expected. Conversely, there was an upregulation of hormonal (estrogen response), Notch, cell-cell adhesion, epithelial-mesenchymal transition (EMT), and inflammatory signaling pathways in NACT tumors (Figure S5A). When performing differential binding-enrichment analysis between treatment-naive and NACT tumors on the open chromatin, we found that 9 of 14 (64%) ovarian-specific MTFs[4] were differentially enriched in NACT tumor open chromatin regions (Figure 4D).

Next, we performed a similar analysis on the sensitive and the resistant groups within the treatment-naive tumor samples, where we observed that stress-associated genes were also significantly upregulated in resistance (Figures 4E and 4F). Epigenomic analysis revealed that 10 of 14 ovarian-specific MTFs (71%) were differentially enriched in patients who developed chemotherapy resistance (Figure 4G). Looking for molecular similarities between NACT (residual) samples and resistant tumors, we found that 89 genes (4%) were common in GEX, while 649 DBFs (62%) were overlapping in epigenomic enrichment (Figure 4H). Following this observation, we defined the top 100 DBFs that were most significantly enriched in open chromatin regions common to NACT and resistant tumors as the PCS (Figures 4I and S5B–S5D; Table S6).

The distribution of the PCS score, quantified as the aggregate enrichment score of all 100 DBFs in each cell (Figure S5E), showed a significant increase between sensitive and resistant cells and between resistant and NACT cells (Figure 4J), validating our approach to identifying the molecular signature that likely confers persistence potential to certain cells. Upon assigning cell states based on PCS scores, i.e., PCS-high state and PCS-low state defined as the upper and lower quartiles of PCS scores, respectively, we found that the proportion of cells in these PCS states followed similar trends despite patient variability (Figure 4K).

Functional characterization and validation of the PCS

We then characterized the factors that comprise the PCS based on their function and known associations with ovarian cancer. Overall, the signature consisted of 63 TFs with known motifs, including many members of the basic leucine zipper (bZIP), basic-helix-loop-helix (bHLH), and zinc-finger (ZF) families (Figure 5A). The TFs in the signature included 22 TFs with established roles in ovarian cancer, including MECOM, PAX8, WT1, SOX17, and ESR1, and TFs linked to cancer stemness, such as SOX2 and KLF4. Several of the factors in the signature are responsive to hormonal signaling (AR and ESR1), including PGR, which has been linked to HGSOC progression and metastasis.[33] Additionally, 37 members of the PCS were chromatin regulators. These included families of chromatin remodelers; histone readers, such as BRD2, BRD4, and BRD9; histone writers, such as EP300 and CREBBP; and erasers, including HDAC1, HDAC2, and KDM1A. The activity of these factors together may be dysregulated to promote a persister-like state in malignant epithelial cells that may drive resistance to chemotherapy. The full persister signature DBFs and their features are listed in Table S7.

Comparison of the pairwise correlation of DBF enrichment between naive tumors and residual disease highlights the cooperativity of the factors that comprise the PCS (Figure 5B). In contrast to naive disease, the PCS was more tightly correlated with NACT and mostly inversely correlated with all other DBFs. Together, the cooperative patterns of these DBFs in the epigenetic signature and their targets may be responsible for the change in cell state toward a persister fate. Interestingly, cells with high PCS scores came from multiple lineages of epithelial cells (Figures S6A and S6B), indicating that the potential for persistence is not apparent in the GEX profile. Of note, the cycling cell cluster showed the lowest average PCS score.

To test whether the PCS scores have the potential to predict the chemoresponse in an independent external cohort of patients with ovarian cancer, we calculated the PCS scores in the snATAC-seq data from metastatic omental patient samples before NACT treatment[22] (Figures 5C and 5D). Notably, we observed that patients with higher average PCS scores before treatment showed worse overall survival, whereas the patient with the lowest PCS score had no recurrence.

Another validation of the PCS came from the enrichment of its factors in ATAC-seq profiles of established ovarian cancer cell lines.[34–37] Cell lines with higher carboplatin IC50 values[38] had higher relative PCS enrichment (Figure 5E). Using OVCAR8, which exhibited the highest PCS enrichment, as a model for chemoresistance, we tested epigenetic drugs that targeted the top chromatin factors in our signature (Figure 5F). These included inobrodib and A-485, which inhibit the histone acetyltransferases CREBBP and EP300[39]; the selective bromodomain and extra terminal (BET) inhibitor I-BET-762, which targets BRD2/4[40]; and the HDAC1/2 inhibitor CUDC-101.[41] We also targeted the Notch pathway transcriptional core factors MAML1 and RPBJ using the gamma secretase inhibitor MK-0752.[42] Additionally, because our signature contained multiple components of the SWI/SNF chromatin remodeling complex (ARID1A, SMARCB1, and SMARCA4), we included the EZH2 inhibitor tazemetostat[43] due to the synthetic lethal relationship between SWI/SNF deficiency and PRC2/EZH2 deficiency.[44] After calculating the drug response for each compound individually (Figure S6C; Table S8), we combined the treatment with carboplatin (Figures 5G and S6D) to identify epigenetic dependencies of chemoresistant ovarian cancer (Table S8). In OVCAR8 cells, combining carboplatin with either inobrodib or I-BET-762 significantly reduced the average carboplatin IC50 compared to carboplatin alone. This suggests that, by inhibiting CREBBP/EP300 and BRD2/4, respectively, both inobrodib and I-BET-762 may preferentially target chemoresistant cells enriched in the PCS.

Multi-omic inference of downstream pathways regulated by the PCS

Building on these results, we next sought to define the downstream pathways from predicted targets of the PCS. Using FigR to combine both GEX and ATAC data, we built regulatory networks identifying genes that are predicted to be activated or repressed by TFs within the PCS (Figures 6A and 6B). From this analysis, we found that the PCS was largely driving the changes in GEX between the groups we compared. Since each of these target genes was regulated by more than one factor, we looked at the ratio between their activating and repressing relationships to determine if each gene was predicted to be more activated or

more repressed (Figures S7A). A large set of genes upregulated in NACT samples (n = 435) was mostly PCS activated, while a subset of downregulated genes in NACT samples (n = 385) was PCS repressed. Pathway analysis on these PCS-target genes revealed that cell-cycle-associated pathways were repressed, and pathways associated with transcriptional misregulation in cancer and the response to stress and stimuli were activated (Figures S7B and S7C). To understand if the predicted targets of the PCS could help us identify the pathways that have been implicated in response to chemotherapy, we compared the targets of our persister TFs to known gene signatures identified in residual HGSOC or associated with quiescence in other tumors[19,25] and our own NACT/resistant overlapping genes. The top gene signatures that were most activated were cytokine, NACT/resistant genes, interferon signaling processes, and stress-associated genes (Figure 6C). The signature also showed considerable activation of pathways related to Notch signaling, EMT, PI3K/AKT, and quiescence, which have been linked to chemoresistant states.[19,32] Of note, the overlap of the PCS targets with the majority of the NACT/resistant genes (61/89) observed in our cohort supports the idea that the epigenome is also driving these changes upstream. Importantly, progression-free survival (PFS) analyses on the PCS-target genes overlapping stress, EMT, and quiescence-associated genes showed significantly worse survival of patients with high expression (Figure 6D; Table S9).

Pre- and post-chemotherapy analysis of the PCS in PDX models of HGSOC

One of the limitations of the analysis of our patient cohort is the absence of paired samples before and after chemotherapy. In order to modulate treatment and test the significance of our persister signature before and after the carboplatin/paclitaxel regimen, we used PDXs.[45,46] HGSOC tumors from three different patients were grafted in immunocompromised mice and treated with 3–4 cycles of chemotherapy. Tumor tissue from each PDX was collected before treatment (untreated) and after the therapeutic regimen (treated) and sequenced via single-nucleus multi-omic profiling (Figure 7A). The models were from patients who presented with high-stage and high-grade disease (Figure S8A). Based on the changes in tumor size following treatment over time, the PDXs were classified as sensitive (PDX 27), stable disease (PDX 235), and resistant (PDX 626) (Figure 7B). After filtering out host mouse cells based on GEX (Figures S8B–S8D) and quality control (Figures S8E and S8F), we obtained high-quality data for 10,591 human cancer cells. Unsupervised clustering, batch-correction, marker analysis, and HPCA reference-mapping approaches helped us identify subpopulations, such as cycling and ciliated cells (Figures S9A–S9F).

Cells with high PCS scores were distributed across multiple lineages of epithelial cells (Figures S10A and S10B). Mitochondrial DNA variants also show that the clonality of the samples does not change considerably with chemotherapy treatment, suggesting non-genetic mechanisms underlying the tumor response to chemotherapy (Figure S10C). There was a significant increase in the average PCS scores across the three untreated PDX models, with scores increasing from sensitive to stable to resistant (Figure S10D). Overall, there was also an increase in the PCS score in treated tumors compared to untreated PDX tumors (Figure S10E). Cell-state assignments based on PCS scores revealed that, following treatment, the proportion of cells in the PCS-high state increased in the sensitive PDX (PDX 27), whereas

the resistant tumor (PDX 626) contained a high proportion of cells in the PCS-high state both before and after treatment (Figure 7C). The increased proportion of cells in a PCS-high state following treatment in PDX 27 was also followed by changes in cooperativity of the DBFs between untreated and residual PDX 27 tumors (Figure S11A). Conversely, the PCS factors were strongly correlated with each other in the resistant PDX 626, which contained the highest proportion of malignant epithelial cells in a PCS-high state, both before and after chemotherapy treatment.

Differential GEX and pathway analysis comparing untreated and treated PDX tumors revealed that cell-cycle-related pathways were downregulated, while angiogenesis and immune signaling responses were upregulated in the residual tumors (Figures S11B and S11C). Differential enrichment of DBFs between untreated and treated PDX tumors revealed that most PCS factors were enriched in the residual PDX tumors (Figure S11D). The same trend was apparent when comparing the untreated sensitive (PDX 27) and resistant (PDX 626) PDX tumors (Figure S11E), corroborating what we observed in the patient cohort. The predicted targets of the PCS largely corresponded with the upregulation of signaling pathways related to angiogenesis, hormonal response, stress response, and changes to cell-cell adhesion (Figures S11F and S11G). Together, these data support the potential of the PCS in predicting the chemotherapy response and suggest that persister-associated genes can change the phenotype of cancer cells to promote mechanisms of cancer resistance.

Finally, by combining expression and chromatin patterns before and after treatment, we identified genes that were epigenetically primed for expression by the PCS before chemotherapy but were only upregulated after chemotherapy (Figures 7D–7F; Table S10). Among the predicted 177 target genes downstream of the PCS, we identified 44 genes that were only upregulated in PCS-high cells when treated with chemotherapy. 33 of these 44 genes were also validated in the human samples by expression patterns (Figure 7E). PFS analysis using these 33 genes showed a significantly worse outcome in patients with high expression of these PCS-primed genes (Figure 7F). Coverage plots around the locus of an example primed gene (*GIPC1*) show the sites with increased accessibility in PCS-high cells compared to PCS-low cells (Figure 7G). The GEX patterns show that *GIPC1* is only upregulated after treatment, even though the epigenetic priming (increase in chromatin accessibility) precedes treatment. Overlaying high-throughput chromosome conformation capture (HiC) data from an HGSOC cell line[12] shows that there is evidence of chromatin looping around these sites in ovarian cancer.

Using these experiments, we show that the PCS separates sensitive and resistant PDX models based on the proportion of cells with a high PCS score before treatment. Moreover, we demonstrate that specific genes in the PCS-high cells can be epigenetically primed by the PCS. These genes stay dormant or lowly expressed before chemotherapy but are significantly upregulated after treatment, which could explain the mechanism by which PCS-high cells gain resistance to chemotherapy.

DISCUSSION

The survival and latent growth activity of chemoresistant cancer cells remains a significant barrier to improving patient outcomes in cancer therapy. Here, we define a PCS that captures the chromatin and transcriptional features of residual HGSOC following chemotherapy. Using single-nucleus epigenomic profiling in a cohort of patient tumors and PDX models, we show that the PCS is enriched in residual disease and predicts the patient response to chemotherapy in treatment-naive tumors. Functionally, the PCS promotes downstream stress-adaptive and survival pathways associated with poor clinical outcomes. Importantly, we show that key PCS components can be therapeutically targeted with epigenetic modulators, representing opportunities to overcome chemoresistance. Together, these findings support a model in which intrinsic epigenetic states underlie the persistence of ovarian cancer cells in the face of chemotherapy treatment.

To date, the investigation of chemoresistance in cancer has primarily focused on genetic mutations, DNA repair deficiencies, and changes at the GEX level.[29,31,32,47,48] However, emerging evidence suggests that epigenetic mechanisms, including changes to chromatin remodeling, may play a pivotal role in cancer development[49] and the persistence of tumor cells following treatment.[5] The ability to perform simultaneous RNA and chromatin accessibility profiling from the same nuclei enabled the direct linkage of regulatory elements to GEX programs. Consistent with recent studies, we have identified changes in chromatin accessibility in tumor cells post-chemotherapy.[22] Further, we show that residual cancer cells following NACT display an enrichment of open chromatin that corresponds with the activity of DBFs implicated in changes to the cell cycle, stress responses, and oncogenic signaling processes. Notably, epigenetic features predictive of persistence were already detectable in treatment-naive tumors, indicating a pre-existing tolerance. These features were associated with genes already upregulated in persister cells prior to treatment but also revealed genes that are epigenetically primed for expression only to be activated upon chemotherapy. In a sensitive PDX model, chemotherapy also induced a shift toward the persister epigenetic state, supporting a tumor adaptive process akin to epigenetic reprogramming and cellular plasticity.

The identification of an enriched signature associated with TFs and chromatin remodelers in residual and chemoresistant HGSOC highlights the need for studying tumor resistance mechanisms at the epigenetic level. Based on our signature, we expect that cancer cells have several mechanisms that allow them to persist in the face of chemotherapy. Specific epigenetic landscapes could enable each cell to choose its appropriate mechanism(s) of survival. The signature consists of TFs involved in the transition of FTs toward oncogenic programs,[7] several members of the AP-1 family linked to stress-adaptive transcriptional responses,[19] antioxidative responses,[5,50] and hormone signaling pathways. Chromatin regulators, including CREBBP, EP300, BRD2/4, and HDAC1/2, were also highly represented, reinforcing that the features of persistence to chemotherapy are orchestrated by changes in the epigenetic landscape.[12] Importantly, the accessibility of several stemness factors, including SOX2, FOXM1, and KLF4, may be influenced by chromatin remodelers in the signature, such as the SWI/SNF chromatin remodeling complex members.[51] Of these, SOX2, in cooperation with JUNB, FOS, and TSC22D1, has already been implicated in

the reactivation of the cell cycle after a reversible cell-cycle arrest observed in quiescent cancer cells.[52,53] Following this model, cells can shift from the quiescent state and then subsequently re-enter the cell cycle to lead to cancer recurrence.[52] In our study, we found cells with high PCS scores from all lineages but a consistently lower average score in cycling populations, supporting a model of transient quiescence.

To directly test the functional importance of the PCS, we identified the CREBBP/EP300 inhibitor inobrodib and the BRD2/4 inhibitor I-BET-762 as pharmacological options to overcome carboplatin resistance. These findings align with previous studies showing that BET inhibitors synergize with carboplatin[54] and poly(ADP-ribose) polymerase inhibitors in chemoresistant states[55] and also suggest that the histone acetyltransferases CREBBP/EP300 represent promising therapeutic targets in ovarian tumors, as has been described in multiple cancers.[39] Together, these results support that chemoresistant states can be therapeutically targeted through specific epigenetic vulnerabilities. Given the high recurrence rates observed in HGSOC, early identification of patients harboring tumors with a high PCS score could facilitate personalized treatment strategies aimed at pre-emptively targeting residual disease.

In conclusion, we have identified potential markers of persister cells in HGSOC at the epigenetic level. Understanding and targeting the mechanisms underlying persister cell survival may reveal new vulnerabilities that could be exploited to delay or prevent cancer recurrence.

Limitations of the study

This study provides important insights into the mechanisms of cancer cell persistence following chemotherapy, but there are several limitations that should be acknowledged. While the findings from the patient cohort were validated in PDX models, additional validation in larger patient cohorts is needed to include different molecular subtypes from HGSOC.[29] Although our cohort includes tumors with and without pathogenic variants in genes related to homologous recombination, it is possible that different genotypes will promote distinct pathways for persistence. The potential of the PCS for early identification of chemotherapy response needs to be evaluated in a larger cohort of patients, but the availability of epigenetic data for such a cohort is a serious limitation at present. The precise mechanisms by which the identified TFs and chromatin regulators drive persister cell survival also remain to be fully elucidated. Future studies should focus on the functional evaluation of the synergistic role of these factors to determine their likelihood to promote the persister state. Additionally, our patient cohort did not include paired tumor samples from before and after chemotherapy, based on the lack of clinical availability of these tissues. The PDX cohort gave us this sequential information in tumors with different responses to chemotherapy, but PDX models do not fully replicate the biology of HGSOC, especially because PDX models lack critical components of the tumor microenvironment.

RESOURCE AVAILABILITY

Lead contact

Requests for further information and resources should be directed to and will be fulfilled by the lead contact, Alexandre Gaspar-Maia (maia.alexandre@mayo.edu).

Materials availability

This study did not generate new unique reagents.

STAR★METHODS

EXPERIMENTAL MODEL AND STUDY PARTICIPANT DETAILS

Patient samples: Fresh tissues from patients with high grade ovarian cancer were collected at the time of primary debulking surgery at Mayo Clinic, Rochester. Written informed consent was obtained from all patients and documented in the electronic medical record. The procedures involving human participants were conducted in accordance with the Declaration of Helsinki. All tumor tissues were coded with a patient heterotransplant (PH) number to protect patient identity in accordance with the Mayo Clinic IRB (09-008768) and in accordance with the Health Insurance Portability and Accountability Act through the Mayo Clinic Ovarian Tumor Repository. Normal human fallopian tube specimens were processed from flash frozen tissue and obtained from the Mayo Clinic Fallopian Tube Organoid Biobank, IRB 18-001967, with study approval under IRB 18-007521.

Patient-derived xenograft models: PDXs were developed by intraperitoneal injection of the donor tumor into female SCID beige mice (C.B.-17/IcrHsd-Prkdcscid Lystbg; Inotiv). Briefly, 0.1 to 0.3 cc of grossly malignant tissue was minced and mixed 1:1 with McCoy's media, supplemented with a one-time dose of Rituximab at the time of initial tumor implantation to reduce the occurrence of spontaneous lymphomas, and injected intraperitoneally. No enzymatic or mechanical tumor dissociation was performed. Mice were monitored by routine palpation for engraftment and tumors were harvested when moribund. PDX models are reported here in accordance to the international minimal information standards. Treatments were started when palpated tumors reached 0.5–1 cm^2. Chemotherapy consisted of carboplatin (51 $mg.kg^{-1}$) and paclitaxel (15 $mg.kg^{-1}$) administered intraperitoneally (IP) once a week. All therapies were administered for 3 or 4 weeks for PH27, PH235, and PH626. The tumor size was assessed weekly by ultrasound; three measurements per session for each animal were made and averaged. All animal procedures were approved by the Mayo Clinic Institutional Animal Care and Use Committee (IACUC), consistent with all policies of the American Veterinary Medical Association.

Cell culture: OVCAR8 ovarian cancer cells were obtained as a generous gift from the Kaufmann lab at Mayo Clinic and were cultured in recommended media (RPMI supplemented with 10% FBS and 1% Penicillin/Streptomycin). Cells were grown in a humidified 37°C incubator with 5% CO_2 and used for dose response experiments within 10 passages. Cells were authenticated (IDEXX bioanalytics) and tested for mycoplasma frequently using the Applied Biological Materials Mycoplasma PCR Detection Kit. For

growth curves, 750 cells were plated in each well of a 96-well plate and their growth was followed for 4 days in Incucyte (Sartorius), with acquisition every 24 h. 24 h after plating, cells were treated with carboplatin alone, carboplatin + DMSO (vehicle controls), or carboplatin + epigenetic therapies targeting the PCS. Each experiment was performed in a technical triplicate (3 wells per dose) with at least 3 independent replicates. Confluency was quantified in each well and the relative confluency to the control was calculated for each experiment on day 4 of culture. IC50s of each individual agent or combination were obtained with non-linear regression analysis using GraphPad Prism (version 10.4.1). Clinical grade carboplatin (Novaplus 61703-360-18) was obtained at the Mayo Clinic Pharmacy. Drugs targeting members of the PCS including A-485 (S8740), I-BET-762 (S7189), inobrodib (S9667), CUDC-101 (S1194) and tazemetostat (S7128) were purchased from Selleckchem.

METHOD DETAILS

Nuclei isolation: Nuclei isolation procedure for Multiome experiments were performed as previously established.[79] Fresh tumor tissue obtained from patients with ovarian cancer after debulking surgery was transferred in a sterile 10 cm culture dish and finely minced using scissors in KRB buffer. The sample was centrifuged at 500 g for 5 min at 4°C, and the supernatant was gently removed without disrupting the pellet. Washes were repeated until the supernatant appeared clear. After the last centrifugation, tissue was aliquoted in cryovials and frozen in liquid nitrogen. On the day of the experiment, frozen tissue was cut into small pieces without thawing and used for the nuclei isolations. For fresh fallopian tube specimens from patients undergoing salpingectomy were collected, single cells were isolated, red blood cells were lysed, and the remaining cells were processed. The nuclei isolation was performed based on the 10x genomics suggested protocol for Complex Tissues for snATAC + snRNA. After mincing, a small piece of tissue the size of rice grain was transferred to a 2 mL microcentrifuge tube containing 300 μL of NP-40 Lysis Buffer and homogenized on ice using a pellet pestle. After adding 1 mL of NP-40 Lysis Buffer, the samples were incubated on ice for either 5 or 30 min. After incubation, the samples were strained using a 70 μm cell strainer, and the flow through was then centrifuged 500*g* for 5 min at 4°C. After centrifugation, the nuclei were permeabilized by resuspending in 100 μL of 0.1X Lysis Buffer and incubating on ice for 2 min. After adding 1 mL of Wash Buffer, the nuclei were centrifuged at 500 g for 5 min at 4°C, and the pellet was resuspended in Diluted nuclei buffer. The nuclei concentration was assessed by PI staining using a Cellometer K2 cell counter. As described below, five thousand nuclei were targeted for capture and used for single nuclei snATAC + snRNA.

Single nuclei snATAC + snRNA-seq: Between 1000 and 8000 nuclei per sample were subjected to transposase assays (exposing buffered nuclei to Tn5 transposase) before proceeding to single-nucleus partitioning into gel beads in emulsion, barcoding, and pre-amplification. ATAC library construction and cDNA, followed by GEX library construction, were done following established 10x Genomics protocols. The libraries concentration was measured using Qubit High Sensitivity assays (Thermo Fisher Scientific), and library profiles were assessed in a fragment analyzer (Advance Analytical) before sequencing. The snATAC and snRNA libraries were sequenced for 50bp paired end sequencing, PE50

and 100PE, respectively on a HiSeq 4000, NextSeq 2000 or NovaSeq X 1.5B instrument (Illumina) before demultiplexing and alignment to the reference genome (GRCh38/hg38).

DNA extraction from patient tumors: Genomic DNA was isolated from snap-frozen tissues samples according to the MasterPure Complete DNA and RNA Purification Kit (Biosearch Technologies MC85200). Briefly ~10 mg of tissue was homogenized in lysis solution containing Proteinase K and incubated with agitation at 65C for 30 min. Samples were subsequently treated with RNase, followed by protein precipitation and then purified DNA was resuspended in TE buffer. NanoDrop spectrophotometry quantified DNA yield and quality.

Data analysis

Multiome data processing: The single nuclei snATAC + snRNA-seq data was processed using data analysis pipeline previously published.[79] Sequenced reads from the gene expression (GEX) and DNA accessibility (ATAC) droplet libraries were aligned and quantified using 10x Genomics Cell Ranger ARC v2.0.0. The reads were aligned to the pre-built human reference genome GRCh38 - v2020-A-2.0.0 (May 3, 2021) provided by 10X Genomics. After quality control, data from each sample was processed using Seurat[56] and Signac functions.[57] GEX and ATAC count matrices from each sample were merged independently using Seurat. GEX count matrix was log-normalized, scaled to mean 0 and variance 1, and dimensionality reduction was performed using PCA on the top 2000 highly variable genes. Uniform manifold approximation and projection (UMAP) for GEX was calculated using the top 50 principal components. Open chromatin peaks called per sample were merged using reduce function from GenomicRanges R package, then the ATAC fragment count matrix was recalculated using Signac. Merged peaks that were smaller than 20 base pairs or larger than 10000 base pairs were removed from analysis. The ATAC count matrix was normalized using Term Frequency - Inverse Document Frequency (TF-IDF) and dimensionality reduction performed using singular value decomposition (SVD) using only peaks with non-zero counts in at least 20 cells - together known as latent semantic indexing (LSI) that generates LSI components. The UMAP for ATAC was calculated using LSI components 2 to 50. Seurat's weighted nearest neighbor (WNN) algorithm was used on principal components 1 to 50 (GEX) and LSI components 2 to 50 (ATAC) together to obtain a combined UMAP projection of both modalities. The integrated data included 70,675 cells from 14 patient samples. Cells with more than 20% of reads mapped to mitochondrial genes, those with less than 200 unique genes detected (GEX), those with less than 200 unique peaks detected (ATAC) and those with transcription start site (TSS) enrichment score (as calculated by Signac) less than 1 were removed for quality control. After QC filtering 52,864 cells were used for all downstream analysis.

Cell type identification: Cell type identification was performed using SingleR[60] in combination with unsupervised clustering using a shared nearest neighbor (SNN) modularity optimization-based clustering algorithm performed by Seurat's FindNeighbors and FindClusters functions. A subset of relevant cell types curated from the Human Primary Cell Atlas[80] reference dataset from celldex was used as the transcriptome reference for SingleR. Clusters that distinctly grouped by patients and contained majority epithelial cells

(as identified by SingleR) were all relabeled as epithelial cells. Markers for each cell type was identified using Seurat's FindAllMarkers function for validating the cell types identified.

Epithelial sub-clustering: To identify sub-populations within epithelial cells, we applied Harmony[61] batch-correction on the GEX matrix containing only the epithelial subset, then performed unsupervised clustering followed by marker identification using Seurat's FindAllMarkers function. The markers were overlapped with known markers to identify known cell sub-populations like cycling, ciliated and secretory cells.

Differential gene expression analysis: Differential gene expression testing in GEX data was performed on the log-normalized counts using Seurat's FindMarkers function with default parameters unless specified otherwise. Wilcoxon rank-sum test with p values adjusted using Bonferroni correction based on the total number of genes in the dataset. Statistically significant differentially expressed genes were selected by keeping only genes that fall below the adjusted p value threshold of 0.05. Differential gene expression testing comparing any two conditions was always done for each cell type independently (although shown together in the volcano plots for efficient visualization), unless specified otherwise. To make sure that the results were not driven by a single patient sample we applied a leave-one-out approach on all tests where we removed cells from one sample at a time redoing the tests and keeping only the genes that passed the adjusted p value threshold in all tests. Pathway analysis was performed using singleseqgset R package. Gene set over-representation analysis on custom gene sets from literature was performed using enricher function from clusterProfiler[81] and over-representation analysis on gene set databases was performed using gprofiler.[65]

Enrichment of DNA binding factors in ATAC data: DNA binding factor enrichment in open chromatin (ATAC) data was estimated using ChromVAR[27] enrichment scores calculated using binding-site data obtained from ReMap2022.[62] Non redundant peaks from the ReMap database was used. Recent data for MECOM, SOX17, PAX8 and WT1 obtained from Nameki et al.,[7] FOXK2 from Zhang et al.,[82] and SOX2 from de Wet et al.[83] were obtained from GEO accession numbers GSE227779, GSE173777 and GSE166183 respectively and appended to the ReMap database before analysis. Differential enrichment between groups of cells was calculated using Seurat's FindMarkers function (Wilcoxon rank-sum test with p values adjusted using Bonferroni correction) on the ChromVAR deviation scores (Z scores).

Persister cell signature: The persister cell signature was defined by performing DNA binding enrichment analysis on open-chromatin regions (peaks) that were differentially accessible in both NACT (vs. naive) and resistant (vs. sensitive) malignant epithelial cells. Differential accessibility testing was performed using Seurat's FindMarkers function (Wilcoxon rank-sum test with Bonferroni correction). ReMapEnrich was then used to calculate the enrichment of all DNA binding factors on the common differentially accessible peaks (n = 1762), and the results were ranked by Q significance. The top 120 DNA binding factors were selected and further filtered by removing factors with very low gene expression.

This is done by selecting only the top 100 factors ranked by percentage of cells expressing each factor in the NACT group. We defined these 100 DNA binding factors as the persister cell signature (PCS). The combined enrichment of all 100 DNA binding factors PCS score per cell was calculated using Seurat's AddModuleScore function. PCS *High* and PCS *Low* cells were defined as cells within the upper and lower quartile of the PCS score distribution, respectively. Curated datasets were used to classify persister signature factors as TFs[28,84] and as chromatin regulators.[85,86]

PCS primed genes: To identify genes that were epigenetically primed for expression by the PCS but are only upregulated after chemotherapy, we started with genes that were predicted by FigR to be targets of transcription factors in the PCS. We then filtered these genes for direct targets of the PCS i.e., only those genes with detectable differentially accessible peaks (more accessible in PCS high cells compared to PCS low cells) within 150 Kb genomic distance from the gene. 177 direct targets of the PCS were differentially expressed in Treated PDX samples compared to the Untreated samples exclusively in the PCS high cells. Among these genes, 44 genes didn't show any difference in expression between PCS *High* and PCS *Low* cells before treatment indicating that these are likely candidate genes that are epigenetically primed in PCS high cells before treatment and are upregulated after chemotherapy treatment. As a sanity check, we removed genes that were inconsistent with the patient data, i.e., those genes that were downregulated in NACT patient samples compared to the naive samples. Finally, we found 33 genes that we analyzed as PCS primed genes that likely confer chemotherapy resistance to cells in the residual tumor. Heatmap for the differentially accessible peaks was plotted with deepTools[87] computeMatrix and plotHeatmap functions using pseudobulk bigwig files exported from the Seurat object and the differentially accessible peaks BED files.

Identification and removal of mouse cells in PDX data: The sequenced reads from the Multiome assay performed on the PDX samples were aligned to both the mouse (mm10) and human (hg38) reference genomes using 10x Genomics Cell Ranger ARC v2.0.0. All downstream processing was performed as described above, on both genomes independently. The fraction of reads that map to mouse genes and the fraction of reads mapping to human genes were calculated per cell. Unsupervised clustering and this fraction were used to determine the cluster of mouse cells.

Prediction of TF regulatory relationships with target genes: The relationship between transcription factors and their target genes were inferred from both GEX and ATAC data by using FigR.[28] FigR combines gene-peak correlation calculated from both modalities to identify domains of regulatory chromatin (DORC) which are gene neighborhoods that likely have high regulatory activity. The algorithm then combined relative enrichment of TF motifs in DORCs and the correlation of TF RNA expression and DORC accessibility to identify TFs that activate or repress different target genes.

Mitochondrial DNA variant analysis: Single-cell mitochondrial DNA genotyping was performed using mgatk[63] on the snATAC data from each sample. Default parameters were

used while running mgatk. Only variants that were confidently detected in more than 5 cells and those with a strand correlation >0.65 were considered after QC.

Copy number variants identification: Numbat[64] was used on the snRNA data from each sample for identifying copy number variants, using default parameters. Cells with posterior probability score >0.55 were considered CNV high, and those with probability <0.45 were considered CNV low, and those in between 0.45 and 0.55 were considered ambiguous.

Co-accessibility plots: Co-accessibility scores between open-chromatin regions in each cell type were calculated using Cicero.[58] The co-accessibility plots around genes were plotted using Seurat's CoveragePlot function.

Enrichment of PCS in ovarian cancer cell lines: Bulk ATAC-seq data for ovarian cancer cell lines were obtained from Gene Expression Obmibus (GEO) - A2780 (GSM4490937, GSM4490938, GSM4490939), Caov3 (GSM3161712, GSM3161713), Kuramochi (GSM7898878, GSM7898879), OVCAR3 (GSM5815615, GSM5815616, GSM5815617), OVCAR8 (GSM3161724, GSM3161725), PEO1 (GSM4490943, GSM4490944, GSM4490945) and PEO4 (GSM4490946, GSM4490947, GSM4490948).[34–37] Reads were trimmed using TrimGalore (with parameter--nextseq 20) then aligned to the hg38 reference genome using bowtie2[72] (with default parameters). High quality alignments (q30) were obtained and sorted using Samtools.[73] Duplicate read mappings were removed using Picard (default parameters). Peaks were called using MACS2[74] (default parameters). Peaks unique to each cell line were then computed using Bedtools.[75] The enrichment of DNA binding factors in each cell line was then calculated using ReMapEnrich. The relative PCS enrichment was estimated by calculating the difference in average enrichment (effect size) between the PCS factors (n = 100) and all other factors (background). Carboplatin IC50s for all cell lines were obtained from publicly available studies.[38,88]

Kaplan-Meier survival analysis: Kaplan-Meier plots displaying the association between gene expression and patient progression-free survival were obtained using KM plotter.[67,89] All serous ovarian subtypes were probed with a survival threshold of 120 months and the best-cutoff was autoselected.

Hi-C data analysis: Hi-C data for OVCAR3 from Kelly et al.[12] was downloaded from GEO accession number GSE174259. Loops were called using Mustache[68] with 5 Kb resolution and p value threshold of 0.05. The hic files were imported and plotted using HiCExperiment[69] and Plotgardener[70] R packages. The coverage plot was generated using Seurat's CoveragePlot and CombineTracks functions. Since the downloaded hic files were in reference to hg19 genome the plots were later aligned using peaks and gene tracks from the coverage plot lifted over to the corresponding genome versions.

Homologous recombination deficiency mutation panel: A customized QIAseq Targeted DNA Pro (Qiagen), covering over 100 genes, was used for ultrasensitive targeted next-generation sequencing (NGS) and DNA library preparation compatible with Illumina platforms. Briefly, 50ng of high-quality genomic DNA - or at least 100ng of DNA extracted from FFPE samples - was fragmented, end repaired, and A-tailed, followed by ligation

with sequencing platform-specific adapters containing unique molecular indices (UMIs). Target enrichment and final library construction were then performed. Unique dual index (UDI) primers were used for sample indexing. The sequencing was carried out on the Illumina NovaSeq X platform. Bioinformatic processing included sample de-multiplexing, FASTQ file trimming, execution of the Sarek DNA pipeline[76] on Google Cloud Platform (GCP), joint genotyping, variant annotation, and formatting. Genetic variants were identified using the Genome Analysis Toolkit (GATK)[77] HaplotypeCaller. Variants with a frequency threshold ≥ 0.01 or read depth <10 were excluded. Variant classification was based on ClinVar[78] when available, otherwise, frameshift and nonsense variants occurring before the nonsense-mediated decay (NMD) cutoff were classified as pathogenic, while all other variants were designated as variants of uncertain significance (VUS).

QUANTIFICATION AND STATISTICAL ANALYSIS

All data acquired in this study are presented as the mean ± SEM from the indicated sample size. We performed statistical analyses and graphs processing using Prism (version 10.4.1) or in R-studio (version 4.3.2). We performed either a two-tailed unpaired Welch's *t* test or the non-parametric Wilcoxon rank-sum test for comparison of two groups depending on the distribution of the data. *p* values less than 0.05 were considered statistically significant. All sample sizes (N) are noted in the figures or corresponding figure legends.

Supplementary Material

Refer to Web version on PubMed Central for supplementary material.

ACKNOWLEDGMENTS

The authors thank the Genome Analysis Core and the Epigenomics Development lab (Mayo Clinic) for technical support and sequencing and Vonda Wall and Katie Karow for help with obtaining patient samples and clinical data. The authors also acknowledge Wayne Croft and Paul Moss for sharing processed data from their study exploring the chromatin landscape of ovarian cancer metastasis.[22] This work was supported by the Mayo Clinic Center for Individualized Medicine; the Mayo Clinic Center for Biomedical Discovery to W.M.I. and A.G.-M.; the NCI Mayo Clinic Ovarian Cancer SPORE grant P50 CA136393 to A.G.-M., N.K., S.H.K., and S.J.W.; and the DOD Ovarian Cancer Research Program, Ovarian Cancer Academy (W81XWH2110475) to A.G.-M. M.G.D. is supported by the Canadian Institutes of Health Research Doctoral Foreign Study Award, the Foundation for Women Wellness, AACR Scholar-in-Training award, and the Mayo Medical Scientist Training Program (T32 GM145408). S.H. is supported by the Paul Calabresi Program in Clinical/Translational Research at the Mayo Clinic Comprehensive Cancer Center (K12CA090628). The Mayo Clinic Genome Analysis Core is supported by P30 CA015083. The graphical abstract was created with BioRender.com.

Data and code availability

- The Multiome (GEX + ATAC) datasets generated and analyzed in this study have been deposited into the NCBI Gene Expression Omnibus (GEO) database (https://www.ncbi.nlm.nih.gov/geo/) with accession number GEO: GSE293459, as listed in the key resources table.
- The code used for analysis can be accessed on GitHub (https://github.com/LabFunEpi/PCS) and on Zenodo (https://doi.org/10.5281/zenodo.17517805), as listed in the key resources table.

- Any additional information required to reanalyze the data reported in this work is available from the lead contact upon request.

REFERENCES

1. Siegel RL, Kratzer TB, Giaquinto AN, Sung H, and Jemal A (2025). Cancer statistics, 2025. CA Cancer J. Clin 75, 10–45. [PubMed: 39817679]
2. Armstrong DK, Alvarez RD, Bakkum-Gamez JN, Barroilhet L, Behbakht K, Berchuck A, Chen LM, Cristea M, DeRosa M, Eisenhauer EL, et al. (2021). Ovarian Cancer, Version 2.2020, NCCN Clinical Practice Guidelines in Oncology. J. Natl. Compr. Canc. Netw 19, 191–226. [PubMed: 33545690]
3. Ozols RF, Bundy BN, Greer BE, Fowler JM, Clarke-Pearson D, Burger RA, Mannel RS, DeGeest K, Hartenbach EM, and Baergen R; Gynecologic Oncology Group (2003). Phase III trial of carboplatin and paclitaxel compared with cisplatin and paclitaxel in patients with optimally resected stage III ovarian cancer: a Gynecologic Oncology Group study. J. Clin. Oncol 21, 3194–3200. [PubMed: 12860964]
4. Reddy J, Fonseca MAS, Corona RI, Nameki R, Segato Dezem F, Klein IA, Chang H, Chaves-Moreira D, Afeyan LK, Malta TM, et al. (2021). Predicting master transcription factors from pan-cancer expression data. Sci. Adv 7, eabf6123. [PubMed: 34818047]
5. Oren Y, Tsabar M, Cuoco MS, Amir-Zilberstein L, Cabanos HF, Hütter JC, Hu B, Thakore PI, Tabaka M, Fulco CP, et al. (2021). Cycling cancer persister cells arise from lineages with distinct programs. Nature 596, 576–582. [PubMed: 34381210]
6. Burdett NL, Willis MO, Alsop K, Hunt AL, Pandey A, Hamilton PT, Abulez T, Liu X, Hoang T, Craig S, et al. (2023). Multiomic analysis of homologous recombination-deficient end-stage high-grade serous ovarian cancer. Nat. Genet 55, 437–450. [PubMed: 36849657]
7. Nameki RA, Chang H, Yu P, Abbasi F, Lin X, Reddy J, Haro M, Fonseca MA, Freedman ML, Drapkin R, et al. (2023). Rewiring of master transcription factor cistromes during high-grade serous ovarian cancer development. eLife 12, RP86360.
8. Mohammed Ismail W, Mazzone A, Ghiraldini FG, Kaur J, Bains M, Munankarmy A, Bagwell MS, Safgren SL, Moore-Weiss J, Buciuc M, et al. (2023). MacroH2A histone variants modulate enhancer activity to repress oncogenic programs and cellular reprogramming. Commun. Biol 6, 215. [PubMed: 36823213]
9. Rheinbay E, Nielsen MM, Abascal F, Wala JA, Shapira O, Tiao G, Hornshøj H, Hess JM, Juul RI, Lin Z, et al. (2020). Analyses of non-coding somatic drivers in 2,658 cancer whole genomes. Nature 578, 102–111. [PubMed: 32025015]
10. Zhang X, and Meyerson M (2020). Illuminating the noncoding genome in cancer. Nat. Cancer 1, 864–872. [PubMed: 35121955]
11. Regner MJ, Wisniewska K, Garcia-Recio S, Thennavan A, Mendez-Giraldez R, Malladi VS, Hawkins G, Parker JS, Perou CM, Bae-Jump VL, and Franco HL (2021). A multi-omic single-cell landscape of human gynecologic malignancies. Mol. Cell 81, 4924–4941.e10. [PubMed: 34739872]
12. Kelly MR, Wisniewska K, Regner MJ, Lewis MW, Perreault AA, Davis ES, Phanstiel DH, Parker JS, and Franco HL (2022). A multi-omic dissection of super-enhancer driven oncogenic gene expression programs in ovarian cancer. Nat. Commun 13, 4247. [PubMed: 35869079]
13. Regner MJ, Garcia-Recio S, Thennavan A, Wisniewska K, Mendez-Giraldez R, Felsheim B, Spanheimer PM, Parker JS, Perou CM, and Franco HL (2025). Defining the regulatory logic of breast cancer using single-cell epigenetic and transcriptome profiling. Cell Genom. 5, 100765. [PubMed: 39914387]
14. Wang Y, Xie H, Chang X, Hu W, Li M, Li Y, Liu H, Cheng H, Wang S, Zhou L, et al. (2022). Single-Cell Dissection of the Multiomic Landscape of High-Grade Serous Ovarian Cancer. Cancer Res. 82, 3903–3916. [PubMed: 35969151]
15. Vázquez-García I, Uhlitz F, Ceglia N, Lim JLP, Wu M, Mohibullah N, Niyazov J, Ruiz AEB, Boehm KM, Bojilova V, et al. (2022). Ovarian cancer mutational processes drive site-specific immune evasion. Nature 612, 778–786. [PubMed: 36517593]

16. Brand J, Haro M, Lin X, Rimel BJ, McGregor SM, Lawrenson K, and Dinh HQ (2024). Fallopian tube single cell analysis reveals myeloid cell alterations in high-grade serous ovarian cancer. iScience 27, 108990. [PubMed: 38384837]

17. Olalekan S, Xie B, Back R, Eckart H, and Basu A (2021). Characterizing the tumor microenvironment of metastatic ovarian cancer by single-cell transcriptomics. Cell Rep. 35, 109165. [PubMed: 34038734]

18. Hornburg M, Desbois M, Lu S, Guan Y, Lo AA, Kaufman S, Elrod A, Lotstein A, DesRochers TM, Munoz-Rodriguez JL, et al. (2021). Single-cell dissection of cellular components and interactions shaping the tumor immune phenotypes in ovarian cancer. Cancer Cell 39, 928–944.e6. [PubMed: 33961783]

19. Zhang K, Erkan EP, Jamalzadeh S, Dai J, Andersson N, Kaipio K, Lamminen T, Mansuri N, Huhtinen K, Carpén O, et al. (2022). Longitudinal single-cell RNA-seq analysis reveals stress-promoted chemoresistance in metastatic ovarian cancer. Sci. Adv 8, eabm1831. [PubMed: 35196078]

20. Buenrostro JD, Corces MR, Lareau CA, Wu B, Schep AN, Aryee MJ, Majeti R, Chang HY, and Greenleaf WJ (2018). Integrated single-cell analysis maps the continuous regulatory landscape of human hematopoietic differentiation. Cell 173, 1535–1548.e16. [PubMed: 29706549]

21. Sundaram L, Kumar A, Zatzman M, Salcedo A, Ravindra N, Shams S, Louie BH, Bagdatli ST, Myers MA, Sarmashghi S, et al. (2024). Single-cell chromatin accessibility reveals malignant regulatory programs in primary human cancers. Science 385, eadk9217. [PubMed: 39236169]

22. Croft W, Pounds R, Jeevan D, Singh K, Balega J, Sundar S, Williams A, Ganesan R, Kehoe S, Ott S, et al. (2024). The chromatin landscape of high-grade serous ovarian cancer metastasis identifies regulatory drivers in post-chemotherapy residual tumour cells. Commun. Biol 7, 1211. [PubMed: 39341888]

23. Kim J, Coffey DM, Creighton CJ, Yu Z, Hawkins SM, and Matzuk MM (2012). High-grade serous ovarian cancer arises from fallopian tube in a mouse model. Proc. Natl. Acad. Sci. USA 109, 3921–3926. [PubMed: 22331912]

24. Miller TE, Lareau CA, Verga JA, DePasquale EAK, Liu V, Ssozi D, Sandor K, Yin Y, Ludwig LS, El Farran CA, et al. (2022). Mitochondrial variant enrichment from high-throughput single-cell RNA sequencing resolves clonal populations. Nat. Biotechnol 40, 1030–1034. [PubMed: 35210612]

25. Patel AP, Tirosh I, Trombetta JJ, Shalek AK, Gillespie SM, Wakimoto H, Cahill DP, Nahed BV, Curry WT, Martuza RL, et al. (2014). Single-cell RNA-seq highlights intratumoral heterogeneity in primary glioblastoma. Science 344, 1396–1401. [PubMed: 24925914]

26. Ulrich ND, Shen Y.-c., Ma Q, Yang K, Hannum DF, Jones A, Machlin J, Randolph JF, Smith YR, Schon SB, et al. (2022). Cellular heterogeneity of human fallopian tubes in normal and hydrosalpinx disease states identified using scRNA-seq. Dev. Cell 57, 914–929.e7. [PubMed: 35320732]

27. Schep AN, Wu B, Buenrostro JD, and Greenleaf WJ (2017). chrom-VAR: inferring transcription-factor-associated accessibility from single-cell epigenomic data. Nat. Methods 14, 975–978. [PubMed: 28825706]

28. Kartha VK, Duarte FM, Hu Y, Ma S, Chew JG, Lareau CA, Earl A, Burkett ZD, Kohlway AS, Lebofsky R, and Buenrostro JD (2022). Functional inference of gene regulation using single-cell multi-omics. Cell Genom. 2, 100166. [PubMed: 36204155]

29. Verhaak RGW, Tamayo P, Yang J-Y, Hubbard D, Zhang H, Creighton CJ, Fereday S, Lawrence M, Carter SL, Mermel CH, et al. (2013). Prognostically relevant gene signatures of high-grade serous ovarian carcinoma. J. Clin. Investig 123, 517–525. [PubMed: 23257362]

30. Millstein J, Budden T, Goode EL, Anglesio MS, Talhouk A, Intermaggio MP, Leong HS, Chen S, Elatre W, Gilks B, et al. (2020). Prognostic gene expression signature for high-grade serous ovarian cancer. Ann. Oncol 31, 1240–1250. [PubMed: 32473302]

31. Matondo A, Jo YH, Shahid M, Choi TG, Nguyen MN, Nguyen NNY, Akter S, Kang I, Ha J, Maeng CH, et al. (2017). The prognostic 97 chemoresponse gene signature in ovarian cancer. Sci. Rep 7, 9689. [PubMed: 28851888]

32. Lahtinen A, Lavikka K, Virtanen A, Li Y, Jamalzadeh S, Skorda A, Lauridsen AR, Zhang K, Marchi G, Isoviita V-M, et al. (2023). Evolutionary states and trajectories characterized by distinct pathways stratify patients with ovarian high grade serous carcinoma. Cancer Cell 41, 1103–1117.e12. [PubMed: 37207655]
33. Kim O, Park EY, Kwon SY, Shin S, Emerson RE, Shin Y-H, De-Mayo FJ, Lydon JP, Coffey DM, Hawkins SM, et al. (2020). Targeting progesterone signaling prevents metastatic ovarian cancer. Proc. Natl. Acad. Sci. USA 117, 31993–32004. [PubMed: 33262282]
34. Osmanbeyoglu HU, Shimizu F, Rynne-Vidal A, Alonso-Curbelo D, Chen H-A, Wen HY, Yeung T-L, Jelinic P, Razavi P, Lowe SW, et al. (2019). Chromatin-informed inference of transcriptional programs in gynecologic and basal breast cancers. Nat. Commun 10, 4369. [PubMed: 31554806]
35. Gallon J, Loomis E, Curry E, Martin N, Brody L, Garner I, Brown R, and Flanagan JM (2021). Chromatin accessibility changes at intergenic regions are associated with ovarian cancer drug resistance. Clin. Epigenetics 13, 122. [PubMed: 34090482]
36. Xu L, Xuan H, He W, Zhang L, Huang M, Li K, Wen H, Xu H, and Shi X (2023). TAZ2 truncation confers overactivation of p300 and cellular vulnerability to HDAC inhibition. Nat. Commun 14, 5362. [PubMed: 37660055]
37. França GS, Baron M, King BR, Bossowski JP, Bjornberg A, Pour M, Rao A, Patel AS, Misirlioglu S, Barkley D, et al. (2024). Cellular adaptation to cancer therapy along a resistance continuum. Nature 631, 876–883. [PubMed: 38987605]
38. Adams KM, Wendt J-R, Wood J, Olson S, Moreno R, Jin Z, Gopalan S, and Lang JD (2025). Cell-intrinsic platinum response and associated genetic and gene expression signatures in ovarian cancer. Cancer Gene Ther. 32, 985–996. [PubMed: 40683954]
39. Sasaki M, Kato D, Yoshida H, Shimizu T, and Ogiwara H (2025). Efficacy of CBP/p300 Dual Inhibitors against Derepression of KREMEN2 in cBAF-Deficient Cancers. Cancer Res. Commun 5, 24–38. [PubMed: 39625239]
40. Mirguet O, Gosmini R, Toum J, Clément CA, Barnathan M, Brusq J-M, Mordaunt JE, Grimes RM, Crowe M, Pineau O, et al. (2013). Discovery of epigenetic regulator I-BET762: lead optimization to afford a clinical candidate inhibitor of the BET bromodomains. J. Med. Chem 56, 7501–7515. [PubMed: 24015967]
41. Shimizu T, LoRusso PM, Papadopoulos KP, Patnaik A, Beeram M, Smith LS, Rasco DW, Mays TA, Chambers G, Ma A, et al. (2014). Phase I first-in-human study of CUDC-101, a multitargeted inhibitor of HDACs, EGFR, and HER2 in patients with advanced solid tumors. Clin. Cancer Res 20, 5032–5040. [PubMed: 25107918]
42. Schott AF, Landis MD, Dontu G, Griffith KA, Layman RM, Krop I, Paskett LA, Wong H, Dobrolecki LE, Lewis MT, et al. (2013). Preclinical and clinical studies of gamma secretase inhibitors with docetaxel on human breast tumors. Clin. Cancer Res 19, 1512–1524. [PubMed: 23340294]
43. Kuntz KW, Campbell JE, Keilhack H, Pollock RM, Knutson SK, Porter-Scott M, Richon VM, Sneeringer CJ, Wigle TJ, Allain CJ, et al. (2016). The importance of being me: magic methyls, methyltransferase inhibitors, and the discovery of tazemetostat. J. Med. Chem 59, 1556–1564. [PubMed: 26769278]
44. Wu S, Fatkhutdinov N, Fukumoto T, Bitler BG, Park PH, Kossenkov AV, Trizzino M, Tang H-Y, Zhang L, Gardini A, et al. (2018). SWI/SNF catalytic subunits' switch drives resistance to EZH2 inhibitors in ARID1A-mutated cells. Nat. Commun 9, 4116. [PubMed: 30297712]
45. Weroha SJ, Becker MA, Enderica-Gonzalez S, Harrington SC, Oberg AL, Maurer MJ, Perkins SE, AlHilli M, Butler KA, McKinstry S, et al. (2014). Tumorgrafts as in vivo surrogates for women with ovarian cancer. Clin. Cancer Res 20, 1288–1297. [PubMed: 24398046]
46. Liu Y, Chanana P, Davila JI, Hou X, Zanfagnin V, McGehee CD, Goode EL, Polley EC, Haluska P, Weroha SJ, and Wang C (2019). Gene expression differences between matched pairs of ovarian cancer patient tumors and patient-derived xenografts. Sci. Rep 9, 6314. [PubMed: 31004097]
47. Patch A-M, Christie EL, Etemadmoghadam D, Garsed DW, George J, Fereday S, Nones K, Cowin P, Alsop K, Bailey PJ, et al. (2015). Whole-genome characterization of chemoresistant ovarian cancer. Nature 521, 489–494. [PubMed: 26017449]

48. The Cancer Genome Atlas Research Network (2011). Integrated genomic analyses of ovarian carcinoma. Nature 474, 609–615. [PubMed: 21720365]
49. Terekhanova NV, Karpova A, Liang W-W, Strzalkowski A, Chen S, Li Y, Southard-Smith AN, Iglesia MD, Wendl MC, Jayasinghe RG, et al. (2023). Epigenetic regulation during cancer transitions across 11 tumour types. Nature 623, 432–441. [PubMed: 37914932]
50. Fox DB, Garcia NMG, McKinney BJ, Lupo R, Noteware LC, Newcomb R, Liu J, Locasale JW, Hirschey MD, and Alvarez JV (2020). NRF2 activation promotes the recurrence of dormant tumour cells through regulation of redox and nucleotide metabolism. Nat. Metab 2, 318–334. [PubMed: 32691018]
51. Wolf BK, Zhao Y, McCray A, Hawk WH, Deary LT, Sugiarto NW, LaCroix IS, Gerber SA, Cheng C, and Wang X (2023). Cooperation of chromatin remodeling SWI/SNF complex and pioneer factor AP-1 shapes 3D enhancer landscapes. Nat. Struct. Mol. Biol 30, 10–21. [PubMed: 36522426]
52. Xie XP, Laks DR, Sun D, Ganbold M, Wang Z, Pedraza AM, Bale T, Tabar V, Brennan C, Zhou X, and Parada LF (2022). Quiescent human glioblastoma cancer stem cells drive tumor initiation, expansion, and recurrence following chemotherapy. Dev. Cell 57, 32–46.e8. [PubMed: 35016005]
53. Fu RZ, Cottrell O, Cutillo L, Rowntree A, Zador Z, Wurdak H, Papalopulu N, and Marinopoulou E (2024). Identification of genes with oscillatory expression in glioblastoma: The paradigm of SOX2. Sci. Rep 14, 2123. [PubMed: 38267500]
54. Yokoyama Y, Zhu H, Lee JH, Kossenkov AV, Wu SY, Wickramasinghe JM, Yin X, Palozola KC, Gardini A, Showe LC, et al. (2016). BET inhibitors suppress ALDH activity by targeting ALDH1A1 super-enhancer in ovarian cancer. Cancer Res. 76, 6320–6330. [PubMed: 27803105]
55. Karakashev S, Zhu H, Yokoyama Y, Zhao B, Fatkhutdinov N, Kossenkov AV, Wilson AJ, Simpkins F, Speicher D, Khabele D, et al. (2017). BET bromodomain inhibition synergizes with PARP inhibitor in epithelial ovarian cancer. Cell Rep. 21, 3398–3405. [PubMed: 29262321]
56. Hao Y, Hao S, Andersen-Nissen E, Mauck WM 3rd, Zheng S, Butler A, Lee MJ, Wilk AJ, Darby C, Zager M, et al. (2021). Integrated analysis of multimodal single-cell data. Cell 184, 3573–3587.e29. [PubMed: 34062119]
57. Stuart T, Srivastava A, Madad S, Lareau CA, and Satija R (2021). Single-cell chromatin state analysis with Signac. Nat. Methods 18, 1333–1341. [PubMed: 34725479]
58. Pliner HA, Packer JS, McFaline-Figueroa JL, Cusanovich DA, Daza RM, Aghamirzaie D, Srivatsan S, Qiu X, Jackson D, Minkina A, et al. (2018). Cicero Predicts cis-Regulatory DNA Interactions from Single-Cell Chromatin Accessibility Data. Mol. Cell 71, 858–871.e8. [PubMed: 30078726]
59. Wickham H (2009). ggplot2, Elegant Graphics for Data Analysis (Springer).
60. Aran D, Looney AP, Liu L, Wu E, Fong V, Hsu A, Chak S, Naikawadi RP, Wolters PJ, Abate AR, et al. (2019). Reference-based analysis of lung single-cell sequencing reveals a transitional profibrotic macrophage. Nat. Immunol 20, 163–172. [PubMed: 30643263]
61. Korsunsky I, Millard N, Fan J, Slowikowski K, Zhang F, Wei K, Baglaenko Y, Brenner M, Loh PR, and Raychaudhuri S (2019). Fast, sensitive and accurate integration of single-cell data with Harmony. Nat. Methods 16, 1289–1296. [PubMed: 31740819]
62. Hammal F, De Langen P, Bergon A, Lopez F, and Ballester B (2022). ReMap 2022: a database of Human, Mouse, Drosophila and Arabidopsis regulatory regions from an integrative analysis of DNA-binding sequencing experiments. Nucleic Acids Res. 50, D316–D325. [PubMed: 34751401]
63. Lareau CA, Ludwig LS, Muus C, Gohil SH, Zhao T, Chiang Z, Pelka K, Verboon JM, Luo W, Christian E, et al. (2021). Massively parallel single-cell mitochondrial DNA genotyping and chromatin profiling. Nat. Biotechnol 39, 451–461. [PubMed: 32788668]
64. Gao T, Soldatov R, Sarkar H, Kurkiewicz A, Biederstedt E, Loh PR, and Kharchenko PV (2023). Haplotype-aware analysis of somatic copy number variations from single-cell transcriptomes. Nat. Biotechnol 41, 417–426. [PubMed: 36163550]
65. Reimand J, Arak T, Adler P, Kolberg L, Reisberg S, Peterson H, and Vilo J (2016). g:Profiler—a web server for functional interpretation of gene lists (2016 update). Nucleic Acids Res. 44, W83–W89. [PubMed: 27098042]

66. Cillo AR, Kürten CHL, Tabib T, Qi Z, Onkar S, Wang T, Liu A, Duvvuri U, Kim S, Soose RJ, et al. (2020). Immune Landscape of Viral- and Carcinogen-Driven Head and Neck Cancer. Immunity 52, 183–199.e9. [PubMed: 31924475]

67. Győrffy B (2024). Transcriptome-level discovery of survival-associated biomarkers and therapy targets in non-small-cell lung cancer. Br. J. Pharmacol 181, 362–374. [PubMed: 37783508]

68. Roayaei Ardakany A, Gezer HT, Lonardi S, and Ay F (2020). Mustache: multi-scale detection of chromatin loops from Hi-C and Micro-C maps using scale-space representation. Genome Biol. 21, 256. [PubMed: 32998764]

69. Serizay J, Matthey-Doret C, Bignaud A, Baudry L, and Koszul R (2024). Orchestrating chromosome conformation capture analysis with Bioconductor. Nat. Commun 15, 1072. [PubMed: 38316789]

70. Kramer NE, Davis ES, Wenger CD, Deoudes EM, Parker SM, Love MI, and Phanstiel DH (2022). Plotgardener: cultivating precise multi-panel figures in R. Bioinformatics 38, 2042–2045. [PubMed: 35134826]

71. Krueger F, James F, Ewels P, Afyounian E, and Schuster-Boeckler S (2021). FelixKrueger/TrimGalore: v0.6.7 - DOI via Zenodo (0.6.7). Zenodo. 10.5281/zenodo.5127899.

72. Langmead B, and Salzberg SL (2012). Fast gapped-read alignment with Bowtie 2. Nat. Methods 9, 357–359. [PubMed: 22388286]

73. Danecek P, Bonfield JK, Liddle J, Marshall J, Ohan V, Pollard MO, Whitwham A, Keane T, McCarthy SA, Davies RM, and Li H (2021). Twelve years of SAMtools and BCFtools. GigaScience 10, giab008. [PubMed: 33590861]

74. Zhang Y, Liu T, Meyer CA, Eeckhoute J, Johnson DS, Bernstein BE, Nusbaum C, Myers RM, Brown M, Li W, and Liu XS (2008). Model-based Analysis of ChIP-Seq (MACS). Genome Biol. 9, R137. [PubMed: 18798982]

75. Quinlan AR, and Hall IM (2010). BEDTools: a flexible suite of utilities for comparing genomic features. Bioinformatics 26, 841–842. [PubMed: 20110278]

76. Hanssen F, Garcia MU, Folkersen L, Pedersen AS, Lescai F, Jodoin S, Miller E, Seybold M, Wacker O, Smith N, et al. (2024). Scalable and efficient DNA sequencing analysis on different compute infrastructures aiding variant discovery. NAR Genom. Bioinform 6, lqae031. [PubMed: 38666213]

77. van der Auwera G, and O'Connor BD (2020). Genomics in the Cloud: Using Docker, GATK, and WDL in Terra, First edition (O'Reilly Media).

78. Landrum MJ, Lee JM, Riley GR, Jang W, Rubinstein WS, Church DM, and Maglott DR (2014). ClinVar: public archive of relationships among sequence variation and human phenotype. Nucleic Acids Res. 42, D980–D985. [PubMed: 24234437]

79. Sandoval L, Mohammed Ismail W, Mazzone A, Dumbrava M, Fernandez J, Munankarmy A, Lasho T, Binder M, Simon V, Kim KH, et al. (2023). Characterization and Optimization of Multiomic Single-Cell Epigenomic Profiling. Genes 14, 1245. [PubMed: 37372428]

80. Mabbott NA, Baillie JK, Brown H, Freeman TC, and Hume DA (2013). An expression atlas of human primary cells: inference of gene function from coexpression networks. BMC Genom. 14, 632.

81. Yu G, Wang L-G, Han Y, and He Q-Y (2012). clusterProfiler: an R Package for Comparing Biological Themes Among Gene Clusters. OMICS 16, 284–287. [PubMed: 22455463]

82. Zhang Y, Wang Y, Zhao G, Tanner EJ, Adli M, and Matei D (2022). FOXK2 promotes ovarian cancer stemness by regulating the unfolded protein response pathway. J. Clin. Investig 132, e151591. [PubMed: 35349489]

83. de Wet L, Williams A, Gillard M, Kregel S, Lamperis S, Gutgesell LC, Vellky JE, Brown R, Conger K, Paner GP, et al. (2022). SOX2 mediates metabolic reprogramming of prostate cancer cells. Oncogene 41, 1190–1202. [PubMed: 35067686]

84. Lambert SA, Jolma A, Campitelli LF, Das PK, Yin Y, Albu M, Chen X, Taipale J, Hughes TR, and Weirauch MT (2018). The human transcription factors. Cell 172, 650–665. [PubMed: 29425488]

85. Zhang Y, Zhang Y, Song C, Zhao X, Ai B, Wang Y, Zhou L, Zhu J, Feng C, Xu L, et al. (2023). CRdb: a comprehensive resource for deciphering chromatin regulators in human. Nucleic Acids Res. 51, D88–D100. [PubMed: 36318256]

86. Ru B, Sun J, Tong Y, Wong CN, Chandra A, Tang ATS, Chow LKY, Wun WL, Levitskaya Z, and Zhang J (2018). CR2Cancer: a database for chromatin regulators in human cancer. Nucleic Acids Res. 46, D918–D924. [PubMed: 29036683]

87. Ramírez F, Ryan DP, Grüning B, Bhardwaj V, Kilpert F, Richter AS, Heyne S, Dündar F, and Manke T (2016). deepTools2: a next generation web server for deep-sequencing data analysis. Nucleic Acids Res. 44, W160–W165. [PubMed: 27079975]

88. Mon MT, Yodkeeree S, Punfa W, Umsumarng S, Lekwanavijit S, Siriaunkgul S, Suprasert P, and Limtrakul P (2017). Relationships of ex-vivo drug resistance assay and cytokine production with clinicopathological features in the primary cell culture of Thai ovarian and fallopian tube cancer patients. Asian Pac. J. Cancer Prev 18, 3063–3071. [PubMed: 29172280]

89. Győrffy B (2024). Integrated analysis of public datasets for the discovery and validation of survival-associated genes in solid tumors. Innovation 5, 100625. [PubMed: 38706955]

Highlights

- Multi-omic snRNA-seq and snATAC-seq profiling of fallopian tubes and ovarian cancer
- Identification of persister signature predictive of patient chemotherapy responses
- Signature drives stress-adaptive and quiescence pathways linked to poor outcomes
- Persister cells are primed for chemotherapy tolerance via chromatin accessibility

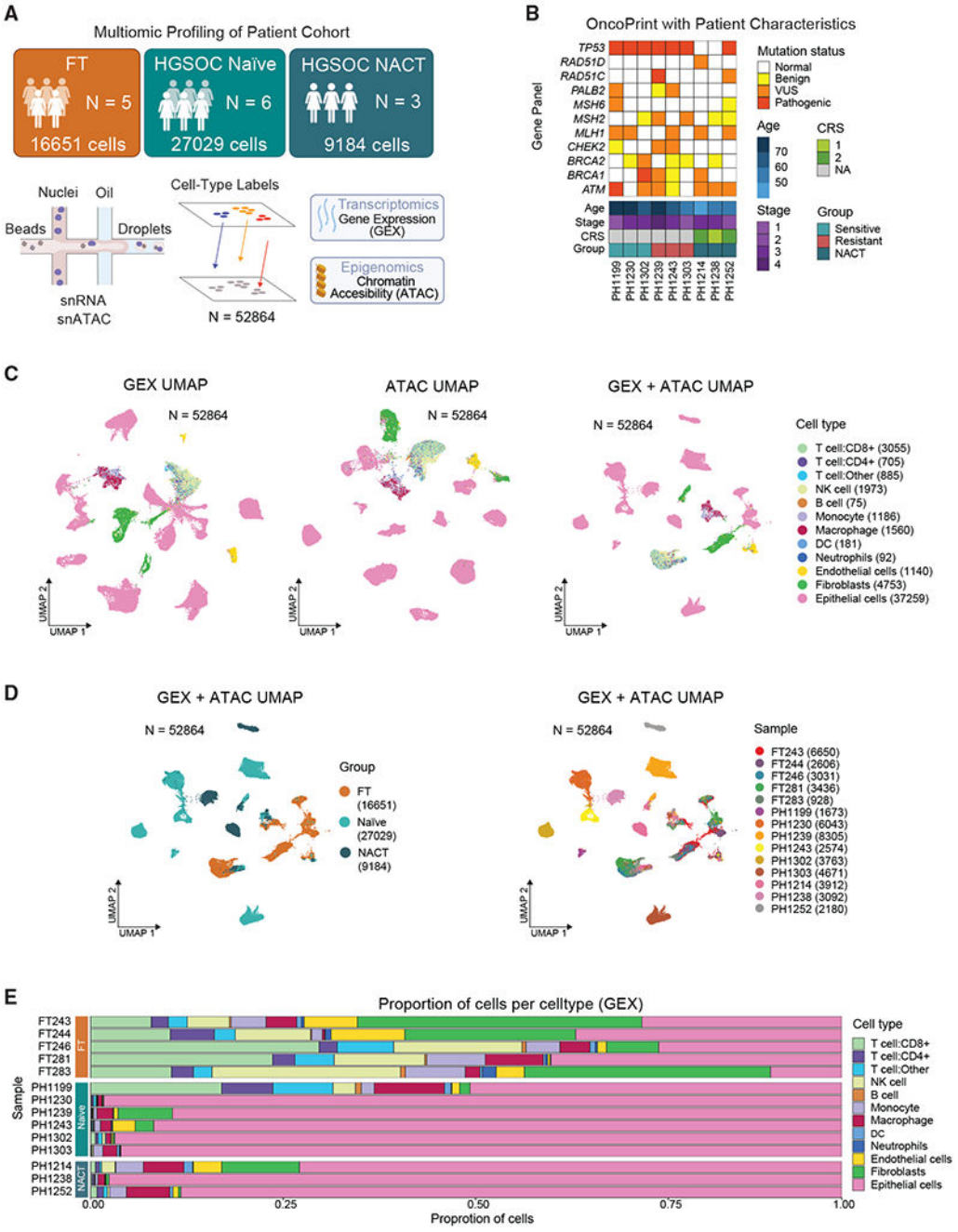

Figure 1. Single-nucleus multi-omic profiling of HGSOC and non-malignant fallopian tubes

(A) Overview of patient cohort consisting of non-malignant fallopian tube (FT) ($n = 5$), naive ($n = 6$), and neoadjuvant chemotherapy (NACT)-treated ($n = 3$) HGSOC tissues and the experimental methodology used for multi-omic snRNA-seq and snATAC-seq profiling. (B) Oncoprint showing gene mutation status and clinical characteristics for each patient. VUS, variant of unknown significance; CRS, chemotherapy response score; NA, not available.

(C) Uniform manifold approximation and projections (UMAPs) of gene expression (GEX), ATAC data, and GEX and ATAC data integrated using weighted nearest neighbor (WNN) approach, colored by cell type.

(D) UMAPs (WNN) colored by group and patient sample. The number of cells (*n*) is shown in brackets.

(E) Bar plots showing the proportion of cells per cell type in each sample.

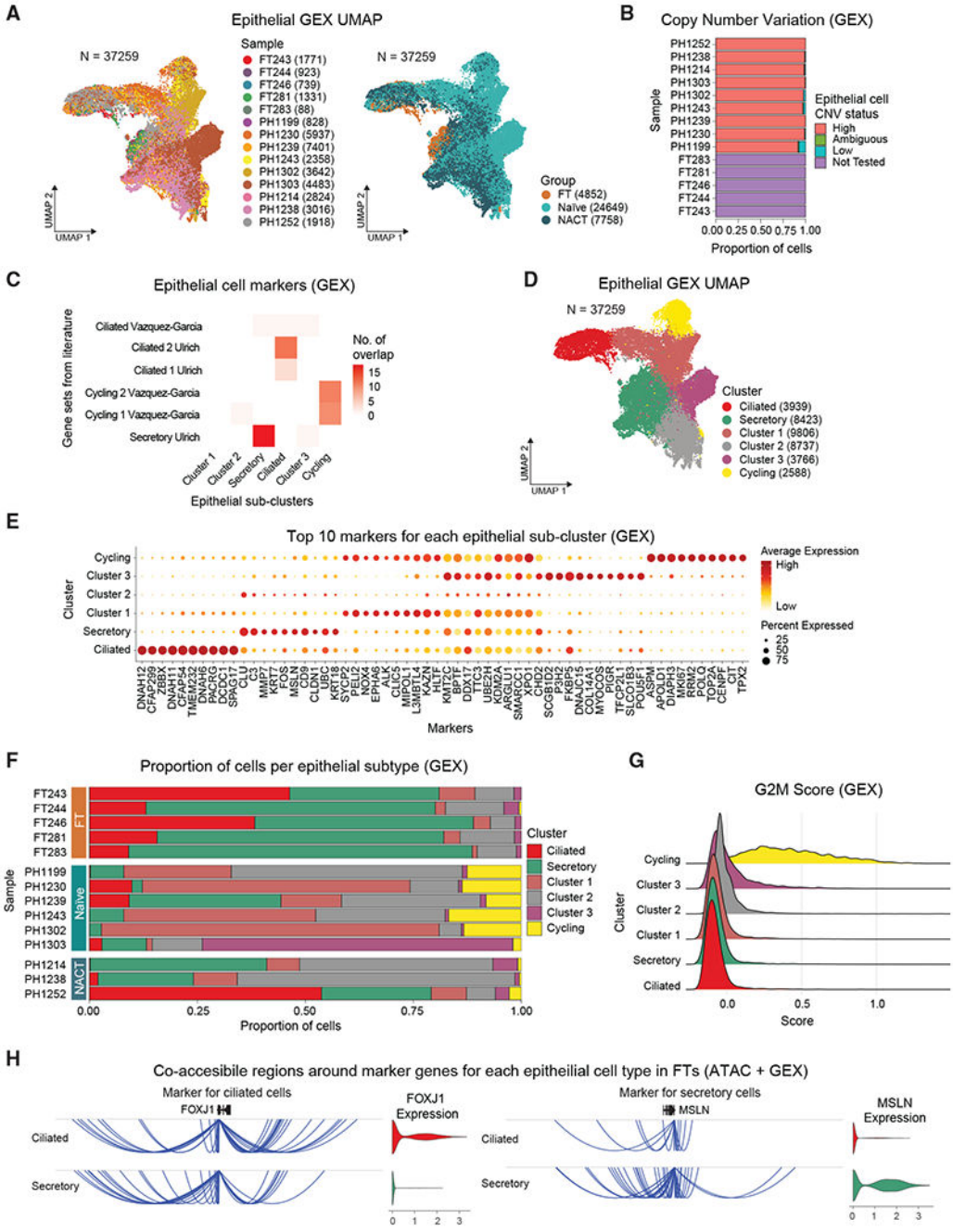

Figure 2. Characterization of epithelial cell subpopulations

(A) UMAP of GEX data from epithelial cells after batch correction using Harmony, colored by sample and by group. The number of cells (*n*) is shown in brackets.

(B) Copy-number variation identified in epithelial cells from each patient sample using Numbat.

(C and D) Epithelial cell subpopulations identified using unsupervised clustering and compared against known markers from literature. The number of cells (*n*) is shown in brackets.

(E) Dotplot showing the top 10 markers of each epithelial subpopulation and their average expression across clusters.
(F) Bar plots showing the proportion of cells per epithelial cell type per sample.
(G) Ridgeplot showing G2M cell cycle phase scores for each cluster based on canonical markers.
(H) Cicero co-accessible sites around marker genes for each epithelial cell type in FTs (FOXJ1 for ciliated and MSLN for secretory cells). The violin plots show the log-normalized GEX.

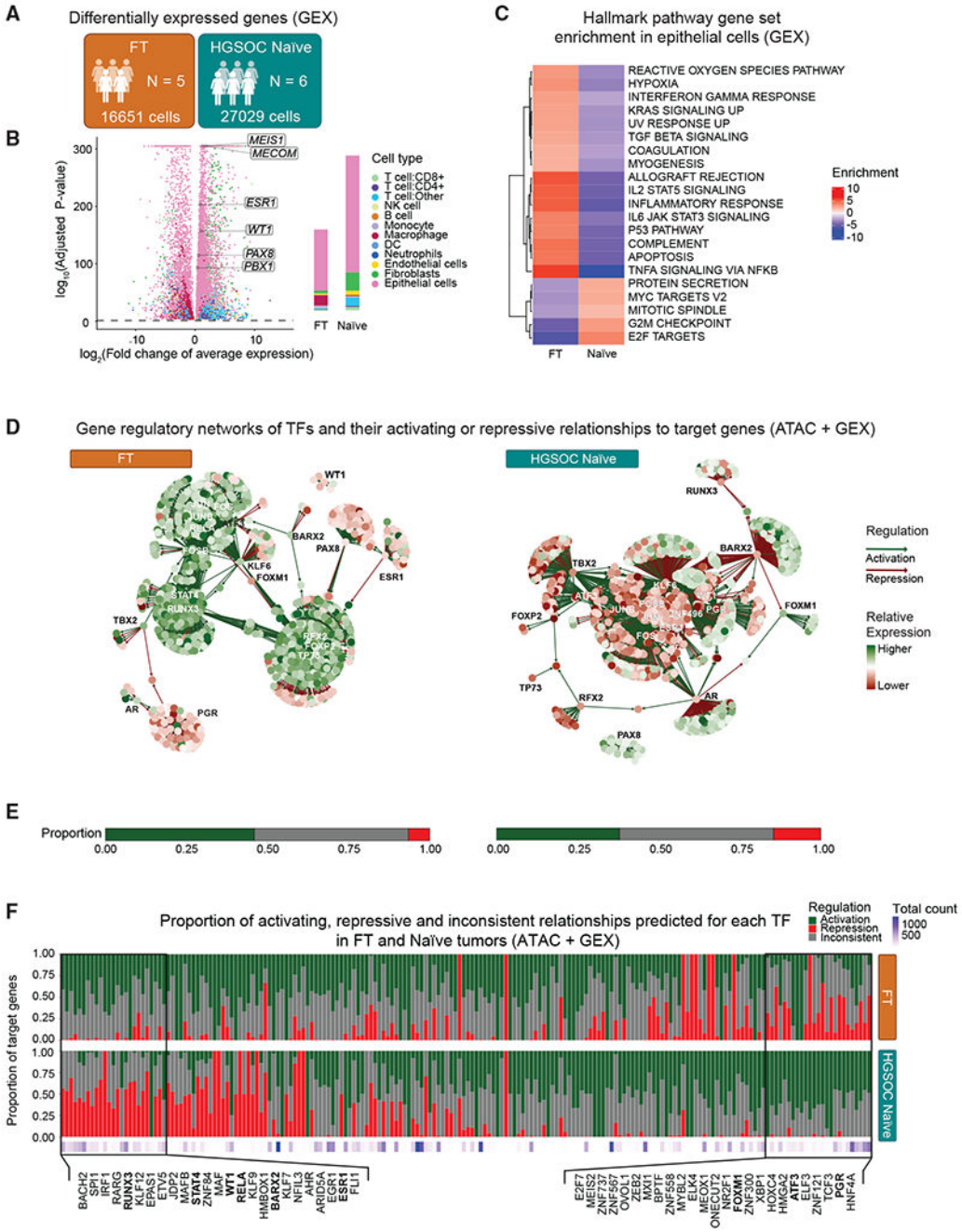

Figure 3. Comparison of transcriptomic and epigenomic programs between non-malignant FTs and HGSOC

(A) Schematic overview of FT ($n = 5$) and naive ($n = 6$) patient cohorts.

(B) Volcano plot showing differentially expressed genes per cell type between FTs and naive tumors. TFs known to play a role in ovarian cancer malignant programs[7] are highlighted. Bar plots on the right show the proportion of genes per cell type upregulated in the FT and naive groups, respectively.

(C) Predicted ontology of Hallmark gene sets enriched in FTs and naive tumors.

(D) Gene regulatory networks (GRNs) highlighting the top TFs that underlie each state and their activating or repressive relationships to their target genes. TF-target gene relationships were inferred using FigR.
(E) Bar plots summarizing the proportion of activating (green), repressive (red), and inconsistent (gray) relationships predicted for all shared TFs in FTs and naive tumors.
(F) Bar plots highlighting the proportion of activating, repressive, and inconsistent relationships for each TF with activity in both FTs and naive tumors based on FigR predictions. The total number of TF-target gene relationships for both FTs and naive tumors is shown as a heatmap on the bottom, and the top 25 TFs with changes in their activity are labeled on each end. TF nodes from FT and naive tumor GRNs are highlighted in bold.

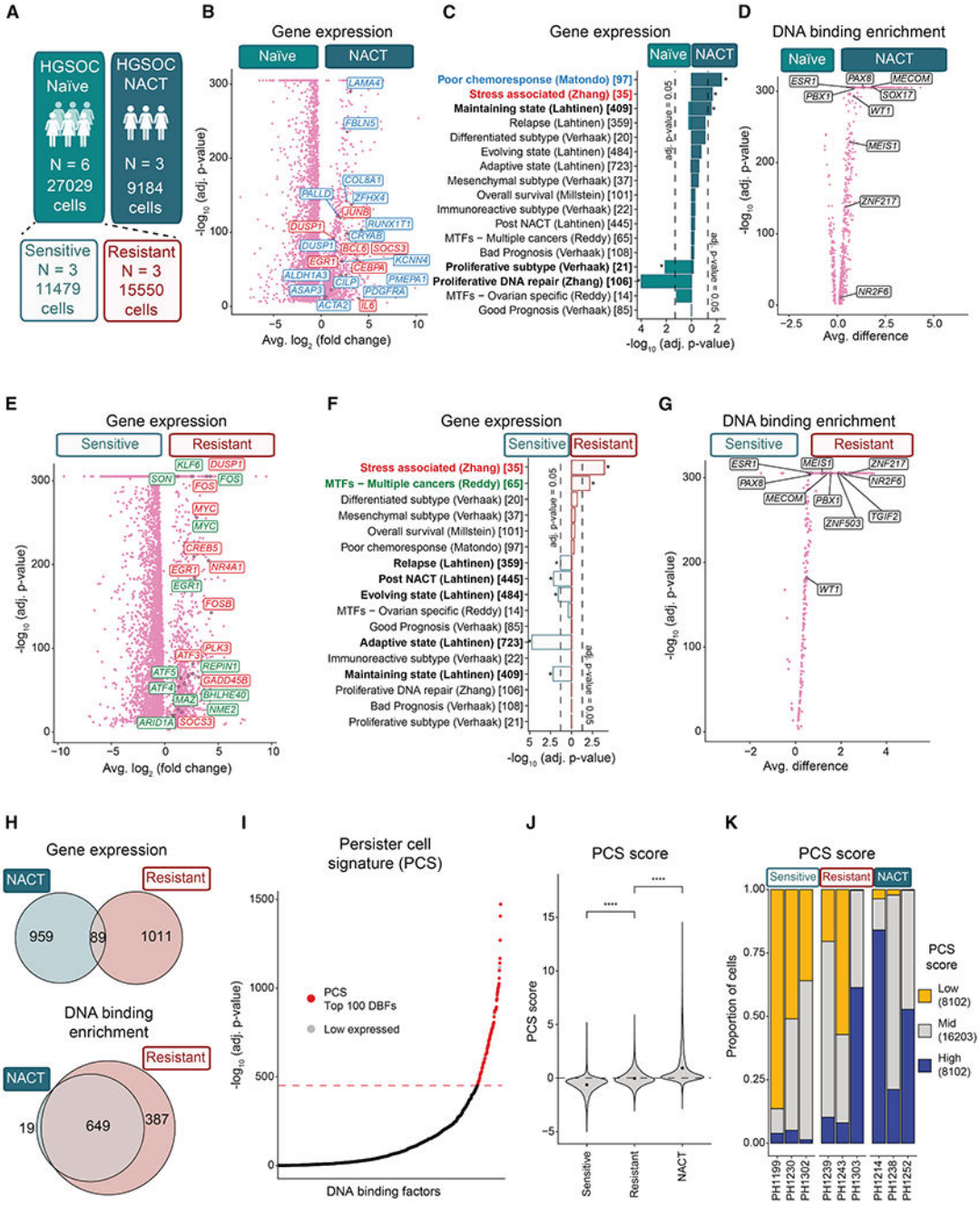

Figure 4. Comparison of NACT and resistant samples reveals a persister cell signature

(A) Schematic overview of naive (n = 6) and NACT (n = 3) patient cohorts, including naive sensitive and resistant.

(B–D) Comparisons between naive and NACT tumors: (B) volcano plot showing differentially expressed genes in epithelial cells. (C) Overlap of gene sets predictive of patient response/outcomes in ovarian cancer and the genes upregulated in naive (n = 3,327) and NACT (n = 1,048) tumors. The number of genes in each gene set is shown in brackets. The statistical significance was calculated using a hypergeometric test with

Benjamini-Hochberg (BH) correction. Significantly enriched gene sets ($p < 0.05$) are shown in bold and with an * next to the bar. (D) Differential enrichment of DNA-binding factors (TFs and chromatin remodelers) in epithelial cells predicted by ChromVAR analysis on snATAC-seq data. Ovarian-specific master transcription factors are highlighted.
(E–G) Comparisons between sensitive and resistant tumors: (E) volcano plot showing differentially expressed genes in epithelial cells. (F) Overlap of ovarian cancer gene sets and the genes upregulated in sensitive ($n = 3,925$) and resistant ($n = 1,100$) groups. The number of genes in each gene set is shown in brackets. The statistical significance was calculated using a hypergeometric test with BH correction. Significantly enriched gene sets ($p < 0.05$) are shown in bold and with an * next to the bar.
(G) Differential enrichment of DNA-binding factors in epithelial cells predicted by ChromVAR analysis. Ovarian-specific master transcription factors are highlighted.
(H) Venn diagrams showing the overlap between NACT and resistant molecular signatures observed in gene expression (top) and DNA-binding enrichment (bottom).
(I) Top 100 DNA-binding factors enriched in open chromatin regions common to both NACT and resistant cells, filtered by highest expression, are defined as the persister cell signature (PCS). Enrichment statistics were calculated using ReMapEnrich.
(J) Violin plots showing the distribution of PCS score per cell between naive sensitive, naive resistant, and NACT tumors. The number of cells (n) in each group is the same as in (A). The dots represent the mean values for each group. Wilcox test ****$p < 0.0001$.
(K) Proportion of cells in PCS-high, -mid, and -low states in each patient. The number of cells (n) is shown in brackets.

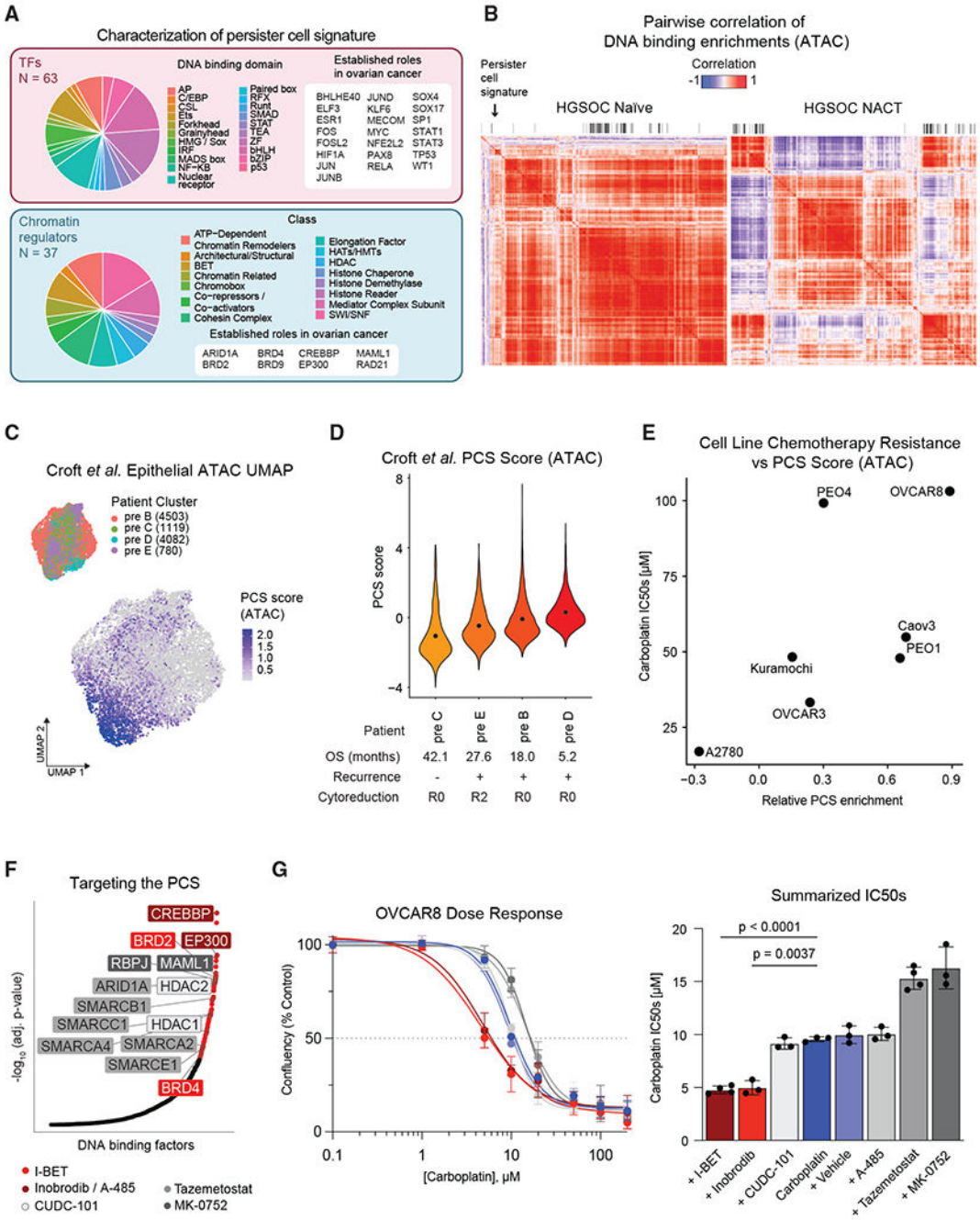

Figure 5. Functional characterization and validation of the PCS

(A) Classification of the persister cell signature into TFs or non-TFs, function, and known association with ovarian cancer.

(B) Differences in pairwise correlation of DNA-binding enrichment scores calculated using ChromVAR between naive tumors and NACT tumors. The members of the PCS are highlighted on top of the images.

(C) Harmony batch-corrected UMAPs of gene activity scores from the snATAC-seq data obtained from Croft et al.[22] colored by patient (inset) and PCS score heatmap. The number of cells (*n*) is shown in brackets.

(D) Violin plots showing the distribution of PCS score per cell between each patient ($n = 4$) from Croft et al. data arranged by overall survival. The dots represent the mean values. The number of cells (*n*) in each group is the same as in (C).

(E) Scatterplot showing the relationship between the relative PCS score and carboplatin IC50s for ovarian cancer cell lines ($n = 7$).

(F) Top 100 DNA-binding factors enriched in open chromatin regions common to both NACT and resistant cells with epigenetic therapies and their potential targets within the PCS. Both inobrodib and A-485 target CREBBP and EP300.

(G) Representative dose response to carboplatin alone and in combination with therapies that target the PCS in OVCAR8 cells after 4 days of treatment. Barplots summarize the data as the mean IC50 of the experiments for each drug ± SEM. Welch's *t* test; *p* values are shown for each comparison. $n \geq 3$ biological replicates.

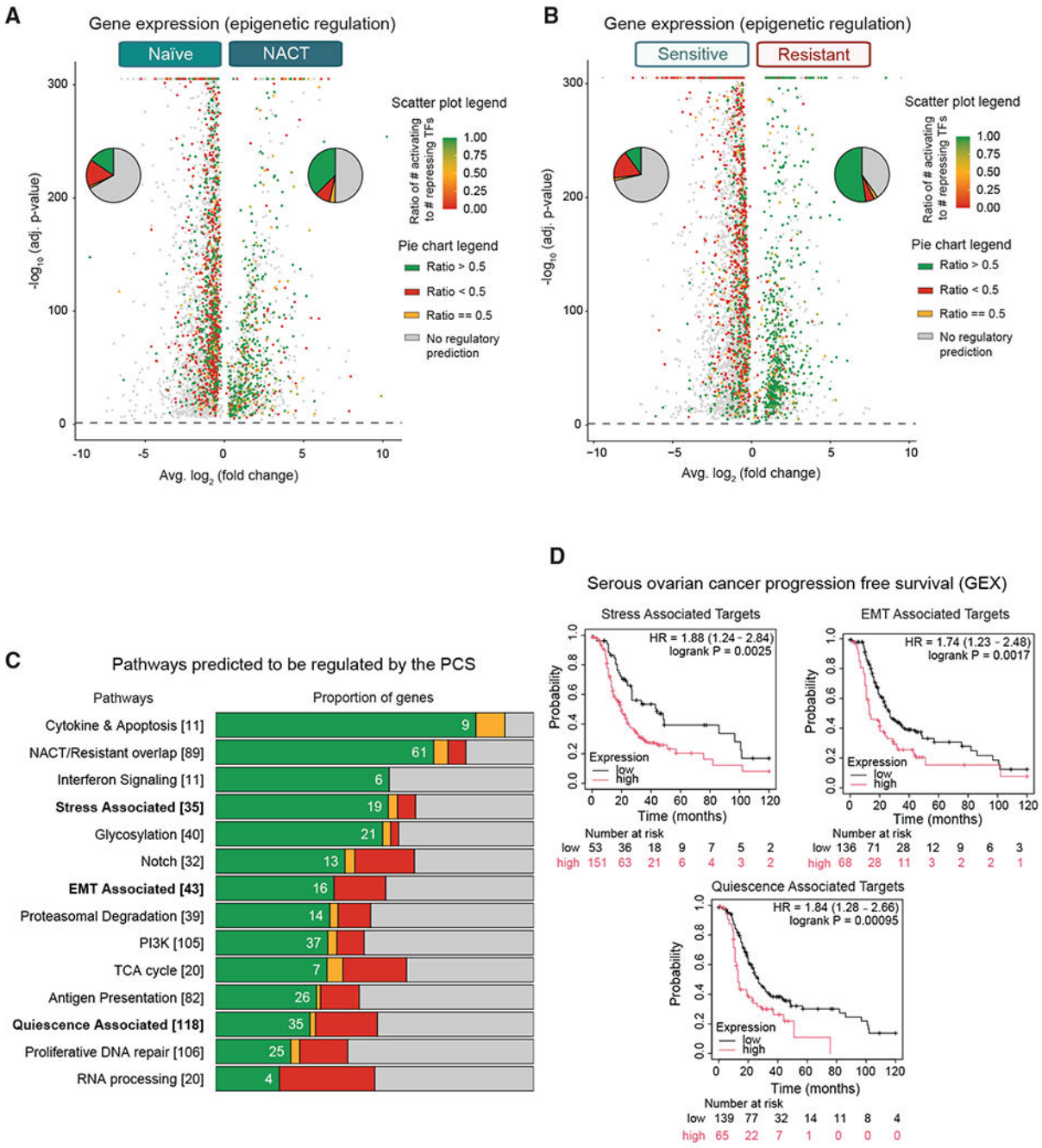

Figure 6. Multi-omic inference of downstream pathways regulated by the PCS

(A and B) Volcano plots showing differentially expressed genes in epithelial cells between naive and NACT tumors (A) and between sensitive and resistant groups

(B), highlighting predicted targets of the PCS transcription factors and their activating or repressive relationships.

(C) Proportion of genes in HGSOC established pathways predicted to be regulated by the PCS using FigR analysis. The number of genes with more activating relationships (green bar) is highlighted in white.

(D) Kaplan-Meier (KM) plots showing the progression-free survival (PFS) from all public datasets used by KM-plotter stratified by the expression of stress-associated, EMT, and quiescence-associated genes that are predicted targets of the PCS. The cohort consists of patients with serous ovarian cancer with optimal debulking. HR, hazard ratio.

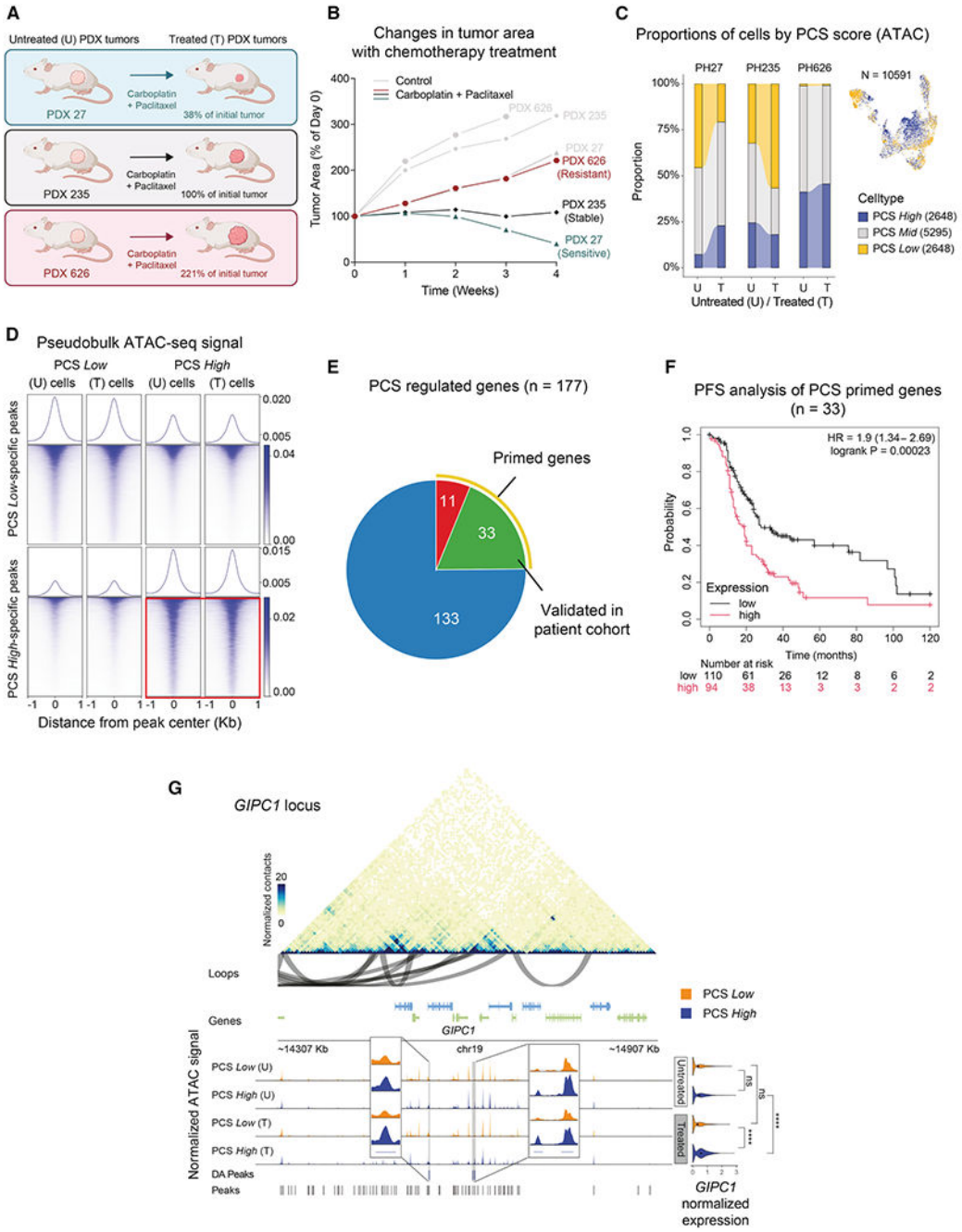

Figure 7. Paired patient-derived xenograft models display an enrichment of the persister cell signature and its downstream signaling pathways following chemotherapy

(A) HGSOC PDX cohort of naive and chemotherapy-treated residual disease analyzed by single-nucleus multi-omic profiling ($n = 6$).

(B) PDX tumors were classified as sensitive, neutral, or resistant based on changes in tumor area following chemotherapy treatment over time.

(C) Sankey plot showing the change in proportion of PCS-high, -mid, and -low cells in each PDX before and after chemotherapy treatment. The PCS-high and -low cells are defined as those cells within the upper and lower quartiles of the PCS score distribution across all cells,

respectively. UMAPs of GEX data from PDX epithelial cells after batch correction using Harmony, colored by PCS-high, -mid, and -low cells, are shown on the right. The number of cells (*n*) in each group is shown in brackets.

(D) Average signal profile and heatmaps showing pseudobulk ATAC signal in differentially accessible (DA) peaks between PCS-high and -low cells.

(E) Pie chart of differentially expressed PCS targets highlighting the primed genes that change only in PCS-high cells when comparing untreated and treated samples.

(F) PFS (KM-plotter) analysis of the 33 primed genes after filtering consistent patterns in the human dataset.

(G) Coverage plot around the *GIPC1* locus showing the normalized ATAC signal per group of cells, the DA peaks, and all peaks from the multiome data. A HiC data heatmap of normalized contacts from OVCAR3 cells is shown (top). Loops called using these data are shown below the heatmap. The violin plots on the right show the log-normalized gene expression of *GIPC1* in each cell group. The dots represent the mean values. Wilcoxon rank sum test; ns, not significant and ****$p < 0.0001$.

KEY RESOURCES TABLE

REAGENT or RESOURCE	SOURCE	IDENTIFIER
Chemicals, peptides, and recombinant proteins		
Nuclei Buffer* (20X)	10x Genomics	PN-2000153
Digitonin	Thermo Fisher Scientific	BN2006
Trizma Hydrochloride Solution, pH 7.4	SigmaAldrich	T2194
Sodium Chloride Solution, 5 M	SigmaAldrich	59222C
Magnesium Chloride Solution, 1M	SigmaAldrich	M1028
Nonidet P40 Substitute	SigmaAldrich	74385
Sigma Protector RNase inhibitor	SigmaAldrich	3335402001
DTT	SigmaAldrich	646563
7-AAD Ready Made Solution	SigmaAldrich	SML1633-1ML
MACS BSA Stock Solution	Miltenyi Biotec	130-091-376
RNase-Free Disposable Pellet Pestles	Fisher Scientific	12-141-368
Tween 20	Bio-Rad	1662404
1X Phosphate-Buffered Saline, pH 7.4	Corning	21-040-CV
RPMI 1640 Medium	Gibco	11875093
Pinnacle Fetal Bovine Serum	Phoenix Scientific	PS-100
Penicillin-Streptomycin	Gibco	15140122
0.05% Trypsin-EDTA	Gibco	25300054
Mycoplasma PCR Detection Kit	Applied Biological Materials	G238
MasterPure Complete DNA & RNA Purification Kit	Biosearch Technologies	MC85200
A-485	Selleckchem	S8740
I-BET-762	Selleckchem	S7189
Inobrodib	Selleckchem	S9667
CUDC-101	Selleckchem	S1194
Tazemetostat	Selleckchem	S7128
Clinical grade carboplatin	Novaplus	NDC 61703-360-18
Critical commercial assays		
Chromium Next GEM Single Cell Multiome ATAC + Gene Expression	10x Genomics	PN-1000283
Chromium Next GEM Chip J	10x Genomics	PN-2000264
Sample Index Plate N, Set A	10x Genomics	PN-3000427
Dual Index Plate TT Set A	10x Genomics	PN-3000431
Deposited data		
Processed snRNA + snATAC-seq data	This Paper	GEO: GSE293459
Raw snRNA + snATAC-seq data	This Paper	GEO: GSE293459
Experimental models: Organisms/strains		
PDX Mouse: C.B.-17/IcrHsd-Prkdcscid Lystbg Use approved by Mayo Clinic Institutional Animal Care and Use Committee (IACUC)	Inotiv	https://www.inotiv.com/research-model/cb-17-icrhsd-prkdcscidlystbg-j

REAGENT or RESOURCE	SOURCE	IDENTIFIER
Experimental models: Cell lines		
OVCAR8 Ovarian Cancer Cell line	Kaufmann lab Mayo Clinic	–
Software and algorithms		
R v4.3.2	The R Project for Statistical Computing	https://www.r-project.org/
CellRanger-ARC v2.0.0	10x Genomics	https://www.10xgenomics.com/support/software/cell-ranger-arc/latest
GRCh38 - v2020-A-2.0.0	10X Genomics	https://cf.10xgenomics.com/supp/cell-arc/refdata-cellranger-arc-GRCh38-2020-A.tar.gz
Seurat v4.0.4	Hao et al.[56]	https://satijalab.org/seurat/index.html
Signac v1.4.0	Stuart et al.[57]	https://stuartlab.org/signac/
Cicero v1.3.5	Pliner et al.[58]	https://github.com/cole-trapnell-lab/cicero-release?tab=readme-ov-file
ggplot2 v3.3.6	Wickham[59]	https://cran.r-project.org/web/packages/ggplot2/index.html
SingleR v3.2	Aran et al.[60]	https://github.com/dviraran/SingleR
Harmony v1.2.3	Korsunsky et al.[61]	https://github.com/immunogenomics/harmony
ChromVAR v1.28.0	Schep et al.[27]	https://github.com/GreenleafLab/chromVAR
ReMap2022	Hammal et al.[62]	https://github.com/remap-cisreg/ReMapEnrich
FigR v0.1.0	Kartha et al.[28]	https://buenrostrolab.github.io/FigR/index.html
Mgatk v0.6.1	Lareau et al.[63]	http://caleblareau.github.io/mgatk
Numbat v1.4.2	Gao et al.[64]	https://kharchenkolab.github.io/numbat/
gprofiler2 v0.2.0	Kolberg et al.[65]	https://biit.cs.ut.ee/gprofiler/gost
Singleseqgset v0.1.2.9000	Cillo et al.[66]	https://arc85.github.io/singleseqgset/
Kaplan-Meier plotter	Győrffy[67]	https://kmplot.com/analysis/
Mustache v1.0.1	Roayaei Ardakany et al.[68]	https://github.com/ay-lab/mustache
HiCExperiment v1.4.0	Serizay et al.[69]	https://bioconductor.org/books/release/OHCA/
Plotgardener v1.15.1	Kramer et al.[70]	https://github.com/PhanstielLab/plotgardener
TrimGalore v0.6.5	Krueger et al.[71]	https://github.com/FelixKrueger/TrimGalore
Bowtie2 v2.3.3.1	Langmead and Salzberg[72]	https://github.com/BenLangmead/bowtie2
Samtools v1.20	Danecek et al.[73]	https://www.htslib.org/
Picard v2.26.10	Broad Institute	https://github.com/broadinstitute/picard
MACS2 v2.2.9.1	Zhang et al.[74]	https://github.com/macs3-project/MACS
Bedtools v2.27.1	Quinlan and Hall[75]	https://bedtools.readthedocs.io/en/latest/index.html
Sarek DNA pipeline v 3.5.1	Hanssen et al.[76]	https://github.com/nf-core/sarek
GATK v4.3	van der Auwera and O'Connor[77]	https://github.com/broadinstitute/gatk
ClinVar	Landrum et al.[78]	https://www.clinicalgenome.org/data-sharing/clinvar/
Analysis code	This paper	https://doi.org/10.5281/zenodo.17517805
Raw and analyzed data	This paper	GEO: GSE293459